JOURNAL OF PETROLOGY | VOLUME 40 | NUMBER 11 | PAGES 1673–1698 | 1999

An Experimental Study of a Lower Proterozoic A-type Granite from the Eastern Amazonian Craton, Brazil

R. DALL'AGNOL[1]*, B. SCAILLET[2] AND M. PICHAVANT[2]

[1]CENTRO DE GEOCIÊNCIAS, UNIVERSIDADE FEDERAL DO PARÁ, CP 1611, 66075-900, BELÉM, PA, BRAZIL
[2]INSTITUT DES SCIENCES DE LA TERRE D'ORLÉANS, CRSCM–CNRS, 1A RUE DE LA FÉROLLERIE, 45071 ORLÉANS CEDEX 2, FRANCE

RECEIVED JULY 31, 1998; REVISED TYPESCRIPT ACCEPTED MAY 4, 1999

The Jamon granite is representative of the Lower Proterozoic (1·88 Ga) oxidized A-type granites of the eastern part of the Amazonian craton. The dominant facies is a metaluminous to slightly peraluminous hornblende biotite monzogranite with K_2O/Na_2O between 0·8 and 1·5 and $FeO_t/(FeO_t + MgO)$ between 0·8 and 0·9. In contrast to many other A-type granites, the Jamon granite is characterized by early hornblende crystallization and the presence of magnetite. Crystallization experiments were performed on glass at 300 MPa between 700 and 900°C for various melt H_2O contents and for both oxidizing and reducing fO_2 [NNO (nickel–nickel oxide) + 2·5 and NNO – 1·5 on average]. For NNO + 2·5 and under H_2O-rich conditions, ilmenite, clinopyroxene, magnetite and hornblende are near-liquidus phases, followed by plagioclase. The orthopyroxene stability field is restricted to high temperatures and H_2O contents in the melt <5 wt %. In contrast, for NNO – 1·5, magnetite and titanite are absent and orthopyroxene (never observed in the granite), clinopyroxene and ilmenite are the liquidus phases. Conditions of crystallization of amphibole, magnetite and plagioclase constrain the initial melt H_2O content to between 4·5 and 6·5 wt %. Plagioclase cores crystallized from 870 to 720°C. Clinopyroxene, amphibole and biotite $Fe/(Fe + Mg)$ values suggest fO_2 around NNO + 0·5 during crystallization of the granite. The demonstration of relatively hydrous conditions and oxidizing fO_2 for the Jamon granite stresses the diversity of A-type magmas in terms of H_2O contents and redox states. The Jamon granite was most probably generated from oxidized Archaean igneous rocks of mafic–intermediate composition.

KEY WORDS: *A-type granite; experiments; Lower Proterozoic; oxygen fugacity; water content*

INTRODUCTION

Proterozoic anorogenic granites are found in several cratonic areas, such as in the Fennoscandian shield (Nurmi & Haapala, 1986; Haapala & Rämö, 1990; Rämö & Haapala, 1991), in North America (Bridgwater & Windley, 1973; Barker *et al.*, 1975; Van Schmus *et al.*, 1987; Anderson & Bender, 1989; Gower *et al.*, 1990; Emslie, 1991; Emslie & Stirling, 1993) and Australia (Wyborn *et al.*, 1992; Pollard & Mitchell, 1995). They are widespread in several tectonic provinces of the Amazonian craton, which is now recognized as one of the world's major provinces of anorogenic magmatism (Dall'Agnol *et al.*, 1994, 1999*a*; Bettencourt *et al.*, 1995). Anorogenic Amazonian granites have ages ranging from ~1·9 to 1·0 Ga (Machado *et al.*, 1991; Dall'Agnol *et al.*, 1994; Bettencourt *et al.*, 1995) and intrude either Archaean or early to middle Proterozoic sequences. They are petrologically and geochemically diverse, with rock types similar to those found in rapakivi granites from the Fennoscandian shield (Haapala & Rämö, 1992; Rämö & Haapala, 1995). The Amazonian anorogenic granites are classified as A-type (Dall'Agnol *et al.*, 1994, 1999*a*, 1999*b*). Many granite complexes are mineralized (Sn, W, REE, Zr, F, Nb, Be, Ta), and the tin deposits associated with these granites are largely responsible for Brazil becoming a major tin producer in the last 20 years. Given the importance of the province, large time span covered, variety of rock types and the significant mineral resources associated, there is clearly a need for a better petrological understanding of these granites.

*Corresponding author. e-mail: robdal@ufpa.br

The genesis of A-type granites is currently the subject of debate (Collins *et al.*, 1982; Christiansen *et al.*, 1983; Whalen *et al.*, 1987; Creaser *et al.* 1991; Eby, 1992; Landenberger & Collins, 1996; King *et al.* 1997). The various hypotheses for their origin were recently evaluated by Patiño Douce (1997). A-type granites are commonly considered as being reduced [fO_2 < FMQ (fayalite–magnetite–quartz)], as demonstrated unambiguously on some examples (e.g. Emslie & Stirling, 1993; Frost & Frost, 1997); yet relatively oxidized, magnetite-bearing A-type granites can be found in the southwestern part of North America (Anderson & Bender, 1989; Anderson & Smith, 1995), in the Amazonian craton (Magalhães & Dall'Agnol, 1992; Dall'Agnol *et al.*, 1997*a*, 1997*b*, this study) and elsewhere (e.g. Clemens *et al.*, 1986; King *et al.*, 1997). The H_2O content is another crucial factor that is poorly known for A-type magmas. Although they were originally thought to be nearly anhydrous, Clemens *et al.* (1986) and King *et al.* (1997) have argued that the magmas parental to the A-type granites of the Lachlan Fold Belt had H_2O contents of several wt % and consequently are not drier than other granite magma types. At present, only one experimental study has been conducted on a composition typical of A-type granites. Clemens *et al.* (1986) determined the phase relations of an A-type granite from southeastern Australia at 100 MPa and $\log fO_2 =$ FMQ + 0·3. They found magma temperatures of 830°C minimum and melt H_2O contents between 2·4 and 4·3 wt %. However, the late crystallization of amphibole in this granite was not reproduced in these experiments (Clemens *et al.*, 1986).

This paper presents the results of an experimental study undertaken to constrain the magmatic conditions, especially H_2O content and fO_2, of the Jamon granite, an extensively studied massif representative of the oxidized, A-type Proterozoic granites of the Central Amazonian province (Dall'Agnol, 1987; Magalhães & Dall'Agnol, 1992; Dall'Agnol *et al.*, 1994).

GEOLOGICAL SETTING AND FIELD RELATIONS

The Jamon granite is situated in the eastern border of the Amazonian craton and, more precisely, in the Eastern Block of the Central Amazonian Province (Dall'Agnol *et al.*, 1994). The granite body is located in the Archaean Rio Maria Granite–Greenstone Terrane, which corresponds to the southern part of the Carajás Metallogenic Province (Fig. 1). It is intrusive in the Andorinhas Supergroup greenstone belt and the Arco Verde Tonalite and Rio Maria Granodiorite (Dall'Agnol *et al.*, 1997*a*, 1997*c*). The Musa granite is another anorogenic intrusion outcropping in the same region that is very similar to the Jamon granite (Fig. 1). Both granites have associated dykes of rhyolite and dacite porphyry (Gastal, 1987). The Arco Verde Tonalite and the Rio Maria Granodiorite were dated (U–Pb on zircon) at $2957+16/-19$ Ma and $2874+9/-10$ Ma, respectively (Macambira, 1992), whereas metavolcanic rocks of the Andorinhas Supergroup yielded ages of $2904+29/-22$ Ma (Macambira, 1992) and 2979 ± 5 Ma (Pimentel & Machado, 1994). Ages of 1885 ± 32 Ma and $1883+5/-2$ Ma were obtained, respectively, for the Jamon (Pb–Pb, zircon evaporation method; Macambira & Dall'Agnol, 1997) and Musa granites (U–Pb on zircon; Machado *et al.*, 1991). The age of 1·88 Ga is coincident with those obtained in several other anorogenic granites of the Carajás Metallogenic Province, and it is assumed to represent the crystallization age of the Jamon and Musa granites.

The anorogenic granites are unfoliated and contacts with country rocks are very sharp, with the granites cross-cutting the earlier structural trends. The Archaean country rocks are strongly affected by contact metamorphism. The Jamon pluton was emplaced at shallow crustal levels, at pressure ≤300 MPa (Dall'Agnol, 1987; Dall'Agnol *et al.*, 1997*c*), on the basis of Al content in hornblende (see below) and of mineral assemblages developed in the contact aureole.

The Jamon granite is composed of three principal facies in a near-concentric zoning (Fig. 1). The dominant facies, located near the outer border, is a medium-, even-grained, hornblende biotite monzogranite. It grades into a medium-grained or medium- to fine-grained biotite monzogranite concentrated near the centre of the massif. The third facies is a biotite micromonzogranite, probably intrusive in the previously described facies and present only in the central–south. A leucocratic granite, which has very limited distribution, corresponds to the fourth facies. The massif is very poor in enclaves except near its margin, where xenoliths of the country rocks can be found. Dark microgranular enclaves are totally absent.

PETROGRAPHY AND MAGNETIC SUSCEPTIBILITY

The petrography of the Jamon granite was discussed by Dall'Agnol (1987) and Dall'Agnol *et al.* (1997*a*). All facies have monzogranitic modal compositions. The modal percentages of hornblende and biotite and the An content of plagioclase decrease systematically from the hornblende biotite monzogranite to the biotite monzogranite and to the biotite micromonzogranite.

The crystallization sequence of the Jamon granite magma, deduced from microscopic textural criteria, has been discussed by Dall'Agnol (1987) and Dall'Agnol *et al.* (1997*a*; see Fig. 2). Apatite, zircon, ilmenite, magnetite and clinopyroxene (found locally as relics in amphibole)

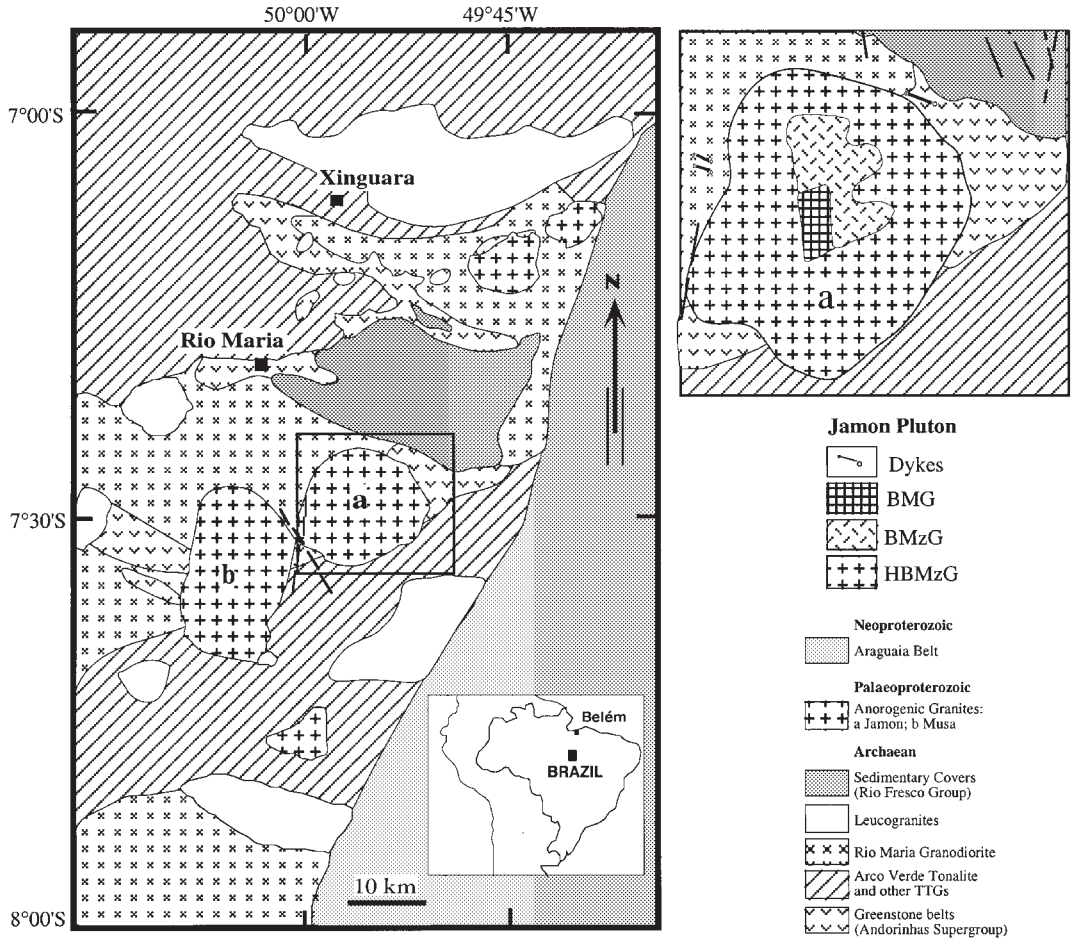

Fig. 1. Geological map of the Rio Maria Granite–Greenstone Terrane showing the location of the Jamon pluton (Dall'Agnol *et al.*, 1997*c*, modified). (a) Jamon pluton; (b) Musa pluton. Inset: detail of the Jamon pluton (Dall'Agnol *et al.*, 1999*b*). HBMzG: hornblende biotite monzogranite; BMzG: biotite monzogranite; BMG: biotite micromonzogranite. The dykes include dacite and rhyolite porphyry dykes.

are the earliest phases in the sequence, and are followed by hornblende and plagioclase. In the hornblende biotite monzogranite, aggregates of relatively calcic plagioclase, hornblende and accessory minerals are common. This sort of aggregate is less common in the biotite monzogranite, where smaller and more sodic plagioclase is present and hornblende is rare. Biotite is later in the sequence and textural relationships suggest that it replaces hornblende. Titanite and allanite crystallize synchronously with the mica and are followed by quartz and alkali feldspar. The Jamon magma is therefore characterized by a relatively early crystallization of the hydrous silicates (Fig. 2). For comparison, biotite is often reported to be an interstitial, near-solidus or subsolidus phase in many other A-type granites (e.g. Clemens *et al.*, 1986; Anderson & Bender, 1989; Emslie & Sterling, 1993). Amphibole, although generally earlier than biotite in the sequence, is also commonly a late phase (e.g. Clemens *et al.*, 1986; Anderson & Bender, 1989; Emslie & Sterling, 1993; King *et al.*, 1997).

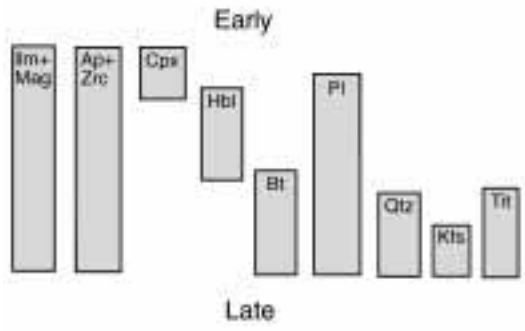

Fig. 2. Crystallization order of the Jamon granite magma as deduced from petrographical observations and rock textures (from Dall'Agnol *et al.*, 1997*a*). Abbreviations as given by Kretz (1983).

All facies have relatively high average modal contents of opaque minerals (>0·5% of both magnetite and ilmenite). Values of magnetic susceptibility for the Jamon granite are similar to those found for the Musa granite and the porphyry dykes, and are higher than those observed for other A-type granites of the Carajás region (Magalhães & Dall'Agnol, 1992; Magalhães *et al.*, 1994). On the basis of the classification of Ishihara (1981), the Jamon is a magnetite-series granite. In comparison, many A-type granites contain ilmenite as the sole Fe–Ti oxide phase (e.g. Emslie & Sterling, 1993; Frost & Frost, 1997; King *et al.*, 1997). Magnetite-bearing A-type granites appear to be less common. In the Lachlan Fold Belt, magnetite-bearing A-type granites are exceptional (Clemens *et al.*, 1986; King *et al.*, 1997). They are relatively common in the Amazonian craton (Magalhães & Dall'Agnol, 1992; Dall'Agnol *et al.*, 1997*a*, 1997*b*, this study) and in the southwestern USA (Anderson, 1983; Anderson & Bender, 1989).

The porphyry dykes have a similar magmatic crystallization history to the Jamon granite. The dacite porphyry dykes have millimetric phenocrysts of idiomorphic plagioclase, clinopyroxene (largely replaced by Al-poor amphibole), abundant opaque crystals (3·1%, including magnetite, subordinate ilmenite and rare secondary pyrite; see Dall'Agnol *et al.*, 1997*a*), rare quartz, hornblende and biotite set in a felsic fine-grained or spherulitic groundmass. In the rhyolite porphyry, the phenocrysts are hornblende, biotite, plagioclase, quartz and alkali feldspar in a felsic fine-grained groundmass; the opaque minerals (2·7%; same phases as in the dacite porphyry) are generally associated with the mafic phenocrysts.

GEOCHEMISTRY

The Jamon granite (Table 1) is subalkaline, metaluminous to slightly peraluminous. K_2O/Na_2O ratios are between 0·8 and 1·5, and $FeO_t/(FeO_t + MgO)$ between 0·8 and 0·9 (concentrations in wt %). Both ratios are lower than those found in other anorogenic granites of the Carajás region. Harker variation diagrams show a gradual transition from the hornblende biotite monzogranite to the biotite micromonzogranite, with K_2O and Rb increasing and CaO, MgO, TiO_2, FeO + Fe_2O_3, Sr and Ba decreasing with increasing SiO_2. The average normative anorthite values and K/Rb ratios decrease in the same way. The three principal Jamon facies have similar contents of rare earth elements (REE), being enriched in light REE (LREE), slightly depleted in heavy REE (HREE) and showing a small negative europium anomaly, which increases from the less evolved to the more evolved facies. Dall'Agnol (1987), Dall'Agnol & Magalhães (1995) and Dall'Agnol *et al.* (1999*b*) proposed that the three principal facies of the Jamon granite are comagmatic and related by fractional crystallization. The porphyry dykes are not comagmatic with the granite, although probably cogenetic.

The Jamon granite has geochemical affinities with A-type granites (Dall'Agnol *et al.*, 1994, 1999*a*, 1999*b*), as defined by Whalen *et al.* (1987). Zr concentrations range between 387 and 164 ppm (Table 1), yielding zircon saturation temperatures (Watson & Harrison, 1983) between 818 and 851°C. For comparison, the average zircon saturation temperature calculated for 55 A-type granites from the Lachlan Fold Belt is 839°C (King *et al.*, 1997). Apatite saturation temperatures (Harrison & Watson, 1984) progressively decrease from the hornblende biotite (802°C) to the biotite monzogranite (740°C), the dacite porphyry yielding higher values (873°C) and the rhyolite porphyry (779°C) being intermediate.

MINERALOGY

Analytical methods

Minerals were analysed at Nancy using a Cameca SX 50 electron microprobe and under the following conditions: 15 kV acceleration voltage, 10 nA sample current, 15 s total counting time. Silicate minerals were used as standards and the data were corrected with the PAP correction program. Analyses for fluorine were carried out under the same conditions, using a PC 1 crystal. Experimental starting materials, minerals and glasses were analysed at Orléans using both a Cameca Camebax and an SX 50 electron microprobe. A sample current of 6 nA was used to minimize alkali migration during glass analysis. Additional details of electron microprobe procedures for experimental products are given below (see also Scaillet *et al.*, 1995; Scaillet & Evans, 1999).

Plagioclase

In all facies, plagioclases are normally zoned, sometimes with an oscillatory character, as best observed in the porphyry dyke samples. Or contents are generally very low in the granite and they reach 2–3% in the porphyry dykes (Table 2). The composition of plagioclases is correlated with the petrographic type. In the hornblende biotite monzogranite, plagioclase cores have compositions between An_{41} and An_{27} (combining the data for different zoned crystals). Border zones have a composition of $An_{\sim 22}$ and local rims of $An_{\sim 12}$. In the biotite monzogranite, most plagioclase crystals display subidiomorphic or idiomorphic cores up to An_{24} and xenomorphic outer zones between An_{16} and An_{10}. Plagioclase cores in the biotite micromonzogranite range between An_{21} and An_{14}. The dacite porphyry dykes contain the most calcic plagioclases

Table 1: Composition of the Jamon granite and comparison with other examples of A-type granites

	Jamon						Watergums	Umiakovik	Hualapai
	HBMzG	Glass*	BMzG	BMG	GP	DP			
wt %									
SiO_2	70·62	72·1	73·71	75·47	71·20	67·93	73·60	72·20	71·00
TiO_2	0·68	0·8	0·35	0·17	0·51	1·12	0·34	0·52	0·35
Al_2O_3	12·92	13·4	12·36	12·50	12·88	12·41	12·44	12·68	13·27
Fe_2O_3	2·00	—	1·48	1·00	3·80	3·46	1·42	0·86	2·41
FeO	2·37	3·7	1·19	0·36	—	4·10	1·49	2·96	—
MnO	0·07	n.d.	0·04	0·01	0·05	0·11	0·08	0·04	0·03
MgO	0·69	0·7	0·32	0·20	0·55	1·11	0·27	0·38	0·31
CaO	2·47	2·2	1·21	0·64	1·79	3·32	1·24	1·54	1·12
Na_2O	3·54	3·8	3·27	3·47	3·47	3·47	3·53	2·80	3·52
K_2O	3·52	3·4	4·75	4·97	4·47	2·93	4·23	5·07	5·81
P_2O_5	0·30	n.d.	0·20	0·13	0·26	0·44	0·07	0·11	n.d.
H_2O_t	0·57	n.d.	n.d.	n.d.	n.d.	n.d.	n.d.	0·58	n.d.
CO_2	0·11	n.d.	n.d.	n.d.	n.d.	n.d.	n.d.	0·13	n.d.
LOI	0·34	—	0·70	0·62	0·67	0·39	n.d.	n.d.	0·95
Total	100·2	100·0	99·58	99·54	99·65	100·76	98·71	99·87	98·77
ppm									
F	1200	n.d.	n.d.	n.d.	n.d.	n.d.	1200	819	n.d.
Rb	108	n.d.	230	281	185	77	201	133	256
Sr	268	n.d.	118	61	197	292	142	158	384
Ba	1399	n.d.	718	443	1100	1230	710	1234	536
Zr	387	n.d.	283	164	328	327	472	496	670
Nb	14	n.d.	21	21	24	13	28	16	28
Ga	24	n.d.	31	28	30	23	21·2	n.d.	17
Y	49	n.d.	79	137	37	45	83	47	33
Ce	95·2	n.d.	178	173	132	122	n.d.	144	n.d.
Sm	10·36	n.d.	13	22	10	11	n.d.	12	n.d.
Eu	2·53	n.d.	1·6	1·9	1·7	2·5	n.d.	2	n.d.
Yb	4·6	n.d.	7·5	10·3	4	3·7	n.d.	4·5	n.d.

Source of data: Jamon (Dall'Agnol *et al.*, 1994; R. Dall'Agnol, unpublished data, 1989), Watergums (Collins *et al.*, 1982; Clemens *et al.*, 1986), Umiakovik (Emslie & Stirling, 1993), Hualapai (Anderson & Bender, 1989). Total Fe as Fe_2O_3 except when otherwise indicated. HBMzG, hornblende biotite monzogranite; BMzG, biotite monzogranite; BMG, biotite micromonzogranite; GP, rhyolite porphyry; DP, dacite porphyry.
*Glass starting material made from the HBMzG sample, electron microprobe analysis recalculated to 100%. Total Fe as FeO.

of the entire suite ($An_{46–40}$, Table 2). In the rhyolite porphyry, plagioclase cores have compositions in the range $An_{32–23}$.

Clinopyroxene

Clinopyroxenes are found only in the hornblende biotite monzogranite and dacite porphyry. They have similar optical, textural and chemical characteristics (Table 3) and are commonly altered. The least altered crystals have compositions of augite and diopside (Morimoto *et al.*, 1988). They have Fe/(Fe + Mg) ratios of 0·44 and ~0·47, respectively, in the hornblende biotite monzogranite and dacite porphyry.

Amphibole

Amphibole occurs in different facies of the Jamon granite and in the rhyolite and dacite porphyry dykes (Table 4). According to the classification of Leake *et al.* (1997), most

Table 2: Representative compositions of natural and experimental plagioclase

	DP		GP		HbMzG		BMzG	
Sample:	CRE106B core	CRE106B rim	CRE106A core	CRE106A rim	AU390 core	AU390 core	AU382 core	AU382 rim
wt %								
SiO_2	57·42	57·94	59·76	62·39	59·40	61·69	63·68	65·72
Al_2O_3	26·56	25·89	24·72	23·78	26·36	24·10	23·71	22·54
FeO	0·60	0·54	0·27	0·23	0·07	0·31	0·24	0·28
CaO	9·29	8·03	6·72	4·89	8·35	5·64	4·78	3·47
Na_2O	5·83	6·22	7·62	8·88	6·66	8·35	8·57	9·46
K_2O	0·45	0·48	0·64	0·17	0·00	0·00	0·00	0·31
Total	100·17	99·20	99·73	100·34	100·84	100·12	100·98	101·78
Structural formulae (16 O)								
Si	5·15	5·23	5·34	5·51	5·25	5·47	5·57	5·70
Al	2·81	2·75	2·61	2·48	2·75	2·52	2·44	2·30
Fe	0·04	0·04	0·02	0·02	0·05	0·02	0·02	0·02
Ca	0·89	0·78	0·65	0·46	0·79	0·54	0·45	0·32
Na	1·02	1·09	1·32	1·52	1·14	1·44	1·46	1·59
K	0·05	0·06	0·07	0·02	0·00	0·00	0·00	0·04
Ab	51·8	56·7	64·8	75·9	59·1	72·8	76·4	81·7
An	45·6	40·4	31·6	23·1	40·9	27·2	23·6	16·5
Or	2·6	2·9	3·6	0·9	0·0	0·0	0·0	1·8
	BMG		Experimental					
Sample:	AU398	AU398	RD35	RD17	RD58	RD3	RD7	RD24
$T°C/fO_2$:	core	rim	899/OXY*	848/OXY	857/RED†	801/OXY	707/OXY	706/RED
wt %								
SiO_2	61·93	65·06	57·48	59·62	59·15	62·44	60·87	60·45
Al_2O_3	23·02	22·51	25·15	24·90	24·20	22·30	24·71	22·98
FeO	n.d.	n.d.	0·86	0·63	0·74	0·93	0·37	1·07
CaO	4·33	2·80	9·12	8·45	7·83	5·28	6·39	5·28
Na_2O	8·91	9·49	5·64	5·67	5·97	7·16	6·69	7·57
K_2O	0·19	0·41	0·57	0·74	0·63	0·97	0·62	0·87
Total	98·38	100·27	98·82	100·02	98·51	99·09	99·65	98·23
Structural formulae (16 O)								
Si	5·57	5·72	5·23	5·33	5·37	5·60	5·43	5·50
Al	2·44	2·33	2·70	2·63	2·59	2·36	2·60	2·46
Fe	—	—	0·07	0·05	0·06	0·07	0·03	0·08
Ca	0·42	0·27	0·89	0·81	0·76	0·51	0·61	0·51
Na	1·55	1·61	1·00	0·98	1·05	1·24	1·16	1·33
K	0·04	0·04	0·07	0·08	0·07	0·11	0·07	0·10
Ab	78·1	84·1	51·0	52·4	55·7	66·8	62·9	68·4
An	20·9	13·8	45·6	43·1	40·4	27·2	33·3	26·4
Or	1·0	2·1	3·4	4·5	3·9	6·0	3·8	5·2

*OXY, NNO + 2·5 (see Appendix A).
†RED, NNO – 1·5 (see Appendix B).
DP, dacite porphyry; GP, rhyolite porphyry; HBMzG, hornblende biotite monzogranite; BMzG, biotite monzogranite; BMG, biotite micromonzogranite.

Table 3: Representative compositions of natural and experimental pyroxene

	HBMzG	DP	Experimental						
Sample:	CRE78A	CRE106B	RD32	RD21	RD64	RD54	RD37	RD64	RD50
T°C/fO_2:			899/OXY*	848/OXY	898/RED†	857/RED	899/OXY	898/RED	801/RED
SiO_2	52·46	51·35	51·44	52·88	53·27	51·87	55·47	53·15	50·41
Al_2O_3	0·78	0·75	2·40	2·69	1·63	1·55	2·45	0·74	1·52
FeO	13·98	15·13	5·49	8·83	11·82	14·15	13·96	21·60	34·34
MgO	10·11	9·50	15·44	13·03	14·36	12·55	22·96	21·34	8·64
MnO	0·88	0·79	0·49	0·00	0·44	0·50	1·76	0·85	0·00
CaO	22·40	20·12	22·87	19·19	16·49	17·22	1·98	1·69	3·89
Na_2O	0·50	0·23	0·45	0·68	0·23	0·26	0·28	0·00	0·18
K_2O	0·07	0·12	0·06	0·46	0·09	0·13	0·38	0·06	0·32
TiO_2	0·11	0·11	0·33	0·53	0·44	0·36	0·41	0·22	0·18
Total	101·29	98·10	98·97	98·30	98·77	98·57	99·64	99·65	99·48
Structural formulae (6 O)									
Si	1·99	2·01	1·92	1·99	2·00	1·98	2·01	1·99	2·02
Al^{IV}	0·01	0·00	0·08	0·01	0·00	0·02	0·00	0·01	0·00
Al^{VI}	0·02	0·03	0·03	0·11	0·07	0·05	0·10	0·02	0·07
Fe	0·44	0·49	0·17	0·28	0·37	0·45	0·42	0·68	1·15
Mg	0·57	0·55	0·86	0·73	0·81	0·72	1·24	1·19	0·52
Mn	0·03	0·03	0·02	0·00	0·01	0·02	0·05	0·03	0·00
Ti	0·00	0·00	0·01	0·02	0·01	0·01	0·01	0·01	0·01
Ca	0·91	0·84	0·91	0·77	0·66	0·71	0·08	0·07	0·17
Na	0·04	0·02	0·03	0·05	0·02	0·02	0·02	0·00	0·01
K	0·00	0·01	0·00	0·02	0·00	0·01	0·02	0·00	0·02
Wo	46·24	41·25	46·05	35·79	30·36	33·50	0·00	2·38	5·44
En	30·31	31·07	45·00	46·56	47·69	40·78	74·92	62·32	29·34
Fs	23·45	27·68	8·95	17·65	21·95	25·72	25·08	35·30	65·22
Fe/(Fe+Mg)	0·44	0·47	0·17	0·27	0·32	0·39	0·25	0·36	0·69

*OXY, NNO + 2·5 (see Appendix A).
†RED, NNO – 1.5 (see Appendix B).
HBMzG, hornblende biotite monzogranite; DP, dacite porphyry.

of the amphibole crystals are ferro-edenitic or edenitic hornblende, with subordinate magnesiohornblende and ferrohornblende. Aluminium-poor amphiboles, classified as actinolite, are found both in the dacite porphyry and locally in the granite, and are late-magmatic to post-magmatic alteration products of clinopyroxene. Hornblende Fe/(Fe + Mg) ratios range from 0·47–0·65 in the hornblende biotite monzogranite to 0·6–0·73 in the biotite monzogranite. In the rhyolite porphyry, the hornblendes are more magnesian, with Fe/(Fe + Mg) ratios of 0·35–0·40 (Table 4). All the analysed amphiboles are relatively rich in fluorine (generally between 1 and 2 wt %) and they contain between 1 and 2 wt % TiO_2. Amphiboles with the highest F concentrations are from the rhyolite porphyry dykes. Hornblende Al_2O_3 contents range between 6 and 8 wt %, and suggest crystallization at upper-crustal pressures (320 ± 70 MPa; see below).

Biotite

The biotites of the different granitic facies and of the rhyolite porphyry dykes are characterized by low Al contents, nearly fully occupied octahedral sites, relatively high F and variable TiO_2 (Table 5). Fe/(Fe + Mg) ratios range from 0·6–0·63 in the hornblende biotite monzogranite to 0·65–0·70 in the biotite monzogranite. In the rhyolite porphyry dykes, the Fe/(Fe + Mg) ratios are remarkably lower (0·4–0·45) than in the granite. Similar values are also found in biotites from the micromonzogranite. As previously noted for amphibole, the

Table 4: Representative compositions of natural and experimental amphibole

	HBMzG			BMzG		GP		Experimental				
Sample:	CRE78A	CRE78A	AU390	AU382	AU382	CRE106A	CRE106A	RD15	RD1	RD7	RD46	RD23
T°C/fO_2:	core	rim	core	core	rim	core	rim	848/OXY*	801/OXY	707/OXY	801/RED†	706/RED
SiO_2	44·80	43·51	44·21	43·99	41·99	46·34	45·74	48·72	48·08	47·14	46·25	44·26
Al_2O_3	6·67	7·39	6·91	6·15	8·08	7·07	7·67	7·25	7·23	7·72	5·92	7·46
FeO	20·74	23·01	19·00	24·10	26·05	13·80	13·87	7·77	11·91	13·24	21·82	24·95
MgO	8·72	7·11	9·74	7·53	5·33	14·12	13·42	17·81	15·40	13·78	9·25	5·74
MnO	0·72	1·07	0·59	1·03	0·95	0·72	0·58	n.d.	0·55	0·58	n.d.	0·58
CaO	10·68	11·17	11·05	11·04	11·15	11·45	11·58	11·38	11·39	10·58	9·65	10·40
Na_2O	1·98	1·88	1·84	1·92	1·79	1·91	2·07	1·59	1·31	1·24	1·31	1·21
K_2O	1·00	1·11	1·34	0·87	1·34	1·14	1·17	0·61	0·60	0·59	0·48	0·56
TiO_2	1·67	1·44	1·81	1·32	0·96	1·60	1·91	1·02	1·05	1·00	1·43	1·13
F	0·97	0·79	1·13	1·55	1·28	2·08	2·12	n.d.	n.d.	n.d.	n.d.	n.d.
Total	97·95	98·48	97·62	99·50	98·92	100·23	100·13	96·15	97·51	95·89	96·11	96·28
Structural formulae (23 O)												
Si	6·92	6·79	6·84	6·87	6·67	6·85	6·78	7·05	7·01	7·02	7·13	6·97
Al	1·21	1·36	1·26	1·13	1·51	1·23	1·34	1·24	1·24	1·36	1·08	1·39
Fe	2·68	3·00	2·46	3·15	3·46	1·71	1·72	0·94	1·45	1·65	2·81	3·29
Mg	2·01	1·65	2·24	1·75	1·26	3·11	2·96	3·85	3·35	3·07	2·13	1·35
Mn	0·09	0·14	0·08	0·14	0·13	0·09	0·07	—	0·07	0·07	—	0·08
Ti	0·19	0·17	0·21	0·15	0·11	0·18	0·21	0·11	0·12	0·11	0·17	0·13
Ca	1·77	1·87	1·83	1·85	1·90	1·81	1·84	1·76	1·78	1·69	1·60	1·76
Na	0·59	0·57	0·26	0·58	0·55	0·55	0·59	0·45	0·37	0·36	0·39	0·37
K	0·20	0·22	0·27	0·17	0·27	0·21	0·22	0·11	0·11	0·11	0·09	0·11
F	0·47	0·39	0·55	0·77	0·64	0·97	0·99	—	—	—	—	—
Fe/(Fe+Mg)	0·57	0·65	0·52	0·64	0·73	0·36	0·37	0·20	0·30	0·35	0·57	0·71

*OXY, NNO + 2·5 (see Appendix A).
†RED, NNO – 1·5 (see Appendix B).
HBMzG, hornblende biotite monzogranite; BMzG, biotite monzogranite; GP, rhyolite porphyry.

highest F contents (2·5–3 wt %, Table 5) are for biotites from the rhyolite porphyry. These biotites also have the lowest TiO_2 contents (1–2 wt %) and they show very high Si in comparison with all the other granite facies. Variations in biotite TiO_2 contents are not correlated with changes of the Fe–Ti oxide assemblage.

Fe–Ti oxides

A detailed study of the texture and chemistry of Fe–Ti oxide minerals was undertaken by Dall'Agnol *et al.* (1997*a*). Magnetite and ilmenite coexist in all granite facies and associated dykes. Primary titanomagnetites have been exsolved into intergrowths of almost pure magnetite and trellis ilmenite. The original titanomagnetite compositions (Table 6) were reconstructed using image analysis (Dall'Agnol *et al.*, 1997*a*). They range from 46% Usp (dacite porphyry) to 28% Usp (rhyolite porphyry) and 20% Usp (hornblende biotite monzogranite). Representative compositions of individual and composite ilmenites range between 20 and 4% Hem (Table 7). Textural and chemical evidence suggests that the compositions of ilmenites from the porphyry dykes are representative of primary magmatic compositions (Dall'Agnol *et al.*, 1997*a*). However, the composition of ilmenites in the granite has been re-equilibrated toward higher Ilm contents during post-magmatic evolution. By using the reconstructed compositions of the titanomagnetites and of ilmenites in the porphyry dykes,

Table 5: Representative compositions of natural and experimental biotite

	HBMzG			BMzG		BMG		GP		Experimental				
Sample:	AU390	AU390	CRE78A	AU382	AU382	AU398	AU398	CRE106A	CRE106A	RD5	RD8	RD20	RD23	RD51
T°C/fO_2:										801/ OXY*	707/ OXY	848/ OXY	706/ RED†	801/ RED
SiO_2	37·17	37·23	37·16	36·82	36·57	37·53	38·58	40·22	40·78	36·01	34·26	36·70	35·65	33·93
Al_2O_3	12·22	12·47	12·12	11·76	12·36	14·61	12·39	11·04	11·10	13·62	15·50	13·00	14·13	13·17
FeO	24·05	25·58	24·30	26·28	27·16	21·34	18·57	19·74	18·10	16·76	19·07	11·88	26·80	22·76
MgO	9·00	8·52	8·64	8·08	6·57	9·26	12·59	13·26	14·43	15·04	14·80	20·74	5·84	9·78
MnO	0·35	0·52	0·39	0·51	0·58	0·67	0·43	0·49	0·44	n.d.	n.d.	n.d.	n.d.	n.d.
Na_2O	0·07	0·07	0·11	0·01	0·00	0·11	0·06	0·00	0·00	0·80	0·55	0·90	0·93	0·49
K_2O	9·51	9·51	9·32	9·16	9·39	9·77	9·61	9·35	9·61	9·36	8·76	9·56	8·48	8·58
TiO_2	3·61	3·61	3·63	2·52	3·08	2·75	2·46	1·73	1·07	4·41	3·06	3·21	4·18	7·28
F	2·05	0·94	1·57	0·87	1·07	n.d.	2·12	2·71	3·00	n.d.	n.d.	n.d.	n.d.	n.d.
Total	98·03	98·45	97·24	96·01	96·79	96·04	96·81	98·54	98·53	96·00	96·00	96·00	96·00	96·00
Structural formulae (22 O)														
Si	5·79	5·74	5·81	5·85	5·80	5·75	5·91	6·09	6·15	5·46	5·23	5·45	5·64	5·29
Al^{IV}	2·21	2·26	2·19	2·15	2·20	2·25	2·09	1·91	1·85	2·43	2·77	2·27	2·36	2·42
Al^{VI}	0·03	0·01	0·04	0·05	0·11	0·39	0·15	0·06	0·12	0·00	0·00	0·00	0·27	0·00
Fe	3·13	3·30	3·18	3·49	3·61	2·73	2·38	2·50	2·28	2·12	2·43	1·47	3·54	2·96
Mg	2·09	1·96	2·01	1·91	1·55	2·11	2·87	2·99	3·24	3·41	3·38	4·60	1·38	2·28
Mn	0·05	0·07	0·05	0·07	0·08	0·09	0·06	0·06	0·06	—	—	—	—	
Ti	0·42	0·42	0·43	0·30	0·37	0·32	0·28	0·20	0·12	0·50	0·35	0·36	0·50	0·85
Na	0·02	0·02	0·03	0·00	0·00	0·03	0·02	0·00	0·00	0·23	0·16	0·26	0·28	0·15
K	1·89	1·87	1·86	1·86	1·90	1·91	1·88	1·81	1·85	1·81	1·71	1·81	1·71	1·71
F	1·01	0·46	0·78	0·44	0·54	—	1·03	1·30	1·43	—	—	—		
Fe/ (Fe+Mg)	0·60	0·63	0·61	0·65	0·70	0·56	0·45	0·46	0·41	0·38	0·42	0·24	0·72	0·57

*OXY, fO_2 at NNO + 2·5 (see Appendix A).
†RED, fO_2 at NNO – 1·5 (see Appendix B).
HBMzG, hornblende biotite monzogranite; BMzG, biotite monzogranite; BMG, biotite micromonzogranite; GP, rhyolite porphyry.

Dall'Agnol *et al.* (1997*a*) obtained temperatures of 775 and 1065°C, respectively, for the rhyolite and dacite porphyry, for fO_2 of NNO (nickel–nickel oxide) + 0·5.

Titanite

Titanite is present locally as individual millimetre-size crystals but is more commonly associated with corroded ilmenite or magnetite crystals (see Dall'Agnol *et al.*, 1997*a*). It is present in all granitic facies, as well as in the porphyry dykes. Most of the titanite crystals have TiO_2 contents around 30–33 wt %, and are relatively rich in Al_2O_3 (3–5 wt %) and F (1–2 wt %). They probably have significant H_2O contents, as suggested by their low probe totals. As observed for biotites and amphiboles, titanites in the rhyolite porphyry dykes are the richest in F.

EXPERIMENTAL STUDY

Choice of experimental conditions

The Jamon granite has the full buffering phase assemblage required for the use of the Al-in-hornblende geobarometer (Hammarstrom & Zen, 1986; Hollister *et al.*, 1987). The hornblende rim compositions of the hornblende biotite monzogranite (Table 4) yield a pressure of 320 ± 70 MPa with the experimental calibration of Schmidt (1992). For comparison, the Johnson & Rutherford (1989) calibration yields a pressure lower by ~100

Table 6: Representative reconstructed compositions of natural and experimental magnetite

	HBMzG		BMzG	DP	GP	Experimental			
Sample:	HZR752	CRE78A	AU382	CRE106B	CRE106A	RD35	RD1	RD6	RD7
T°C/fO_2:						899/OXY[1]	801/0XY	801/OXY	707/OXY
TiO_2	9·10	7·42	8·28	16·37	10·10	1·97	2·82	4·92	1·69
Al_2O_3	0·00	0·22	0·01	0·03	0·04	2·21	1·21	1·53	2·52
Fe_2O_3†	50·56	53·36	51·61	36·90	49·16	62·43	62·12	57·37	62·36
FeO	38·16	36·42	36·76	44·64	38·55	28·13	31·29	33·10	31·29
MgO	0·01	0·01	0·05	0·02	0·02	2·40	1·03	0·73	0·54
MnO	0·93	1·07	1·26	1·38	1·72	0·78	0·75	1·31	0·62
Total	98·76	98·51	97·96	99·34	99·59	97·92	99·21	98·95	99·03
Structural formulae (4 O)									
Al	0·00	0·01	0·00	0·00	0·00	0·10	0·05	0·07	0·11
Fe^{2+}	1·23	1·18	1·20	1·42	1·23	0·90	1·00	1·06	1·00
Fe^{3+}	1·47	1·56	1·51	1·06	1·42	1·79	1·78	1·65	1·79
Mg	0·00	0·00	0·00	0·00	0·00	0·14	0·06	0·04	0·03
Mn	0·03	0·04	0·04	0·04	0·06	0·03	0·02	0·04	0·02
Ti	0·26	0·22	0·24	0·47	0·29	0·06	0·08	0·14	0·05
% Usp‡	25·98	21·36	23·62	46·24	28·22	5·34	7·94	14·18	5·19

*OXY, fO_2 at NNO + 2·5 (see Appendix A).
†Fe_2O_3 from charge balance constraints.
‡% Usp, ulvöspinel content of magnetite calculated following Stormer (1983).
Data for the natural magnetites from Dall'Agnol *et al.* (1997*a*) (see also text). HBMzG, hornblende biotite monzogranite; BMzG, biotite monzogranite; DP, dacite porphyry; GP, rhyolite porphyry.

MPa. Therefore, experiments were all performed at a constant pressure of 300 (± 15) MPa. The underlying assumption is that crystallization of the magma body was for the most part isobaric and occurred at the final level of emplacement of the magma (Dall'Agnol, 1987; see also Clemens *et al.*, 1986, and below). Temperature was varied from 700 to 900°C, to cover most of the crystallization interval. Melt H_2O contents were varied from about 8 wt % (H_2O-saturated conditions for this pressure), down to 2 wt % in the most H_2O-undersaturated runs. Control of the H_2O content of the melt was achieved by varying the composition of the fluid phase (Holtz *et al.*, 1992; Scaillet *et al.*, 1995). A fluid phase (either H_2O or an H_2O–CO_2 mixture) was present in all experiments. The choice of fO_2 was guided by the previous study of Fe–Ti oxides in the Jamon granite, which suggested fO_2 above NNO (Dall'Agnol *et al.*, 1997*a*). However, because many A-type granite magmas evolve under reducing conditions (e.g. Emslie & Stirling, 1993; Anderson & Smith, 1995; Rämö & Haapala, 1995; Frost & Frost, 1997; King *et al.*, 1997), experiments were also conducted at fO_2 < FMQ. Experimental data obtained under either oxidized (NNO + 2·5) or reduced (NNO – 1·5 or FMQ – 0·5) conditions can be compared with the petrographic and mineralogical data for the granite, to constrain the redox conditions.

Experimental techniques

Crystallization experiments were performed on a border facies of the Jamon massif, thought to most closely approximate the composition of the primary liquid (Dall'Agnol & Magalhães, 1995; Dall'Agnol *et al.*, 1997*b*). Natural sample (CRE78A) was ground down to a mesh size of 200 μm, then melted twice at 1400°C and 1 atm for 3 h, with grinding between the melting steps. The resulting glass, ground to 20 μm, was used as starting material in all experiments. The glass composition, determined by electron microprobe analysis, is close to that of the whole-rock analysis obtained on the same sample (Table 1). It is slightly more mafic than the Watergums granite used in the experiments of Clemens *et al.* (1986). For oxidizing conditions, experiments were performed in $Ag_{70}Pd_{30}$ capsules. For reducing conditions, Au capsules were preferred because Fe loss to Au is less important than to AgPd for fO_2 < FMQ, and Au is sufficiently permeable to H_2 above 700°C to allow control of fO_2

Table 7: Representative compositions of natural and experimental ilmenite

	HBMzG		BMzG	DP	GP	Experimental					
	AU390	CRE78A	AU382	CRE106B	CRE106A	RD35	RD1	RD7	RD66	RD46	RD23
T°C/fO_2:						899/OXY*	801/OXY	707/OXY	898/RED†	801/RED	706/RED
TiO_2	49·59	46·69	49·96	41·76	47·38	15·61	22·14	19·22	50·83	50·51	46·29
Al_2O_3	0·00	0·00	0·00	0·01	0·01	0·63	0·37	1·29	0·63	0·21	0·42
Fe_2O_3‡	5·57	7·34	3·00	21·67	9·87	69·77	59·41	61·07	3·70	3·75	5·83
FeO	38·10	34·49	37·57	33·60	37·62	11·49	18·29	16·24	38·93	43·57	40·13
MgO	0·07	0·06	0·02	0·02	0·00	1·28	0·73	0·42	3·13	1·04	0·35
MnO	6·29	7·30	7·23	3·87	4·92	0·26	0·31	0·30	1·20	0·00	0·86
Total	99·62	95·87	97·78	100·91	99·81	99·05	101·25	98·54	98·41	99·08	93·89
Structural formulae (3 O)											
Ti	0·95	0·93	0·97	0·79	0·91	0·31	0·42	0·38	0·96	0·96	0·93
Al	0·00	0·00	0·00	0·00	0·00	0·02	0·01	0·04	0·02	0·01	0·01
Fe^{3+}	0·11	0·15	0·06	0·41	0·19	1·37	1·14	1·20	0·07	0·07	0·12
Fe^{2+}	0·81	0·91	0·81	0·71	0·80	0·25	0·39	0·36	0·81	0·92	0·90
Mg	0·00	0·00	0·00	0·00	0·00	0·05	0·03	0·02	0·12	0·04	0·01
Mn	0·14	0·16	0·16	0·08	0·11	0·01	0·01	0·01	0·03	0·00	0·02
% Ilm§	94·3	92·0	96·8	78·5	90·0	28·80	41·65	37·87	96·20	96·34	93·97

*OXY, fO_2 at NNO + 2·5 (see Appendix A).
†RED, fO_2 at NNO – 1·5 (see Appendix B).
‡Fe_2O_3 from charge balance constraints.
§% Ilm, ilmenite content of rhombohedral oxide calculated following Stormer (1983).
Data for the natural ilmenites from Dall'Agnol *et al.* (1997*a*) (see also text). HBMzG, hornblende biotite monzogranite; BMzG, biotite monzogranite; DP, dacite porphyry; GP, rhyolite porphyry.

(Scaillet *et al.*, 1992). Capsules (1·5 cm length, 0·2 mm wall thickness, and 2·5 mm inner diameter) were loaded first with distilled and deionized H_2O (0–4 mg), then with silver oxalate (0·5–10 mg) as a CO_2 source for the H_2O-undersaturated experiments, and finally with the glass powder (20–25 mg), and were then welded shut.

All experiments were performed in internally heated pressure vessels (IHPV). For experiments under reduced conditions, we used an IHPV equipped with an H_2 membrane (Scaillet *et al.*, 1992, 1995) and pressurized with Ar–H_2 mixtures, whereas oxidizing experiments were carried out in two other vessels pressurized with pure Ar. In all vessels, the temperature was read with between two and four sheathed, type-K thermocouples calibrated at 1 atm against the melting point of NaCl. The overall temperature uncertainty is ± 5°C. Total pressure was continuously monitored with transducers calibrated against a 700 MPa Heise Bourdon tube gauge. Pressure uncertainty is ± 20 bar. All experiments were terminated by switching off the power supply, resulting in a temperature drop of ~200°C over the first 2 min. In oxidizing runs, the oxygen fugacity was monitored with the compositions of coexisting magnetite and ilmenite crystallized during the experiments (see Appendix A). For reducing conditions, the H_2 fugacity (fH_2) was continuously read with a modified Shaw membrane (Scaillet *et al.*, 1992) with an uncertainty in H_2 pressures of ± 1 bar. The oxygen fugacity of these runs was calculated using the H_2O dissociation constant of Robie *et al.* (1978), fugacity coefficients from Shaw & Wones (1964) for H_2 and from Burnham *et al.* (1969) for H_2O. In this paper the redox conditions of the experiments are specified relative to those of the nickel–nickel oxide (NNO) solid buffer, calculated at 300 MPa. Runs performed under oxidizing conditions had fO_2 ranging from NNO + 2·3 up to NNO + 4·3, whereas those under reducing conditions had fO_2 ranging between NNO – 2·19 and NNO – 0·96. For simplicity, in the following, we use the average redox conditions NNO + 2·5 and NNO – 1·5 to characterize the two series of experiments. Run durations varied with temperature, between ~800 and 1050 h at 700°C and ~150 and 300 h at 900°C. Nine runs (five at NNO + 2·5 and four at NNO – 1·5), with a total of 59 individual experimental charges, were performed.

After weighing, capsules were opened and run products directly observed optically under immersion oil to provide a first determination of the phases present. X-ray tech-

niques were used especially for crystal-rich charges, and proved useful to locate the appearance of quartz and alkali feldspar. Parts of the run products were mounted in epoxy and polished for detailed observations with scanning electron microscopy (SEM) and electron microprobe analysis. H_2O contents of experimental glasses were estimated from the difference method (Devine *et al.*, 1995), using a set of eight hydrous glass standards whose H_2O contents are known either from ion probe analyses (Scaillet *et al.*, 1995) or Karl Fischer titration (Holtz *et al.* 1995). Corrections for alkali migration used secondary hydrous glasses of known Na and K contents (e.g. Pichavant, 1987; Scaillet *et al.*, 1995).

Experimental results

Phases present

Details concerning the experimental conditions and run products can be found in Appendices A and B. Crystalline phases identified include plagioclase, quartz, alkali feldspar, hornblende, biotite, clinopyroxene, orthopyroxene and ilmenite. At NNO + 2·5, additional phases present are titanite and magnetite. All phases could be analysed by electron probe but, because of the small sizes of the crystals, recalculation procedures were applied to correct the data for Fe–Ti oxides and biotite for glass contamination (see below). Crystal sizes were mostly between lengths of 10 and 20 μm, except for some hornblende and orthopyroxene crystals, which reached lengths of 50 μm (hornblende) to 100 μm (orthopyroxene) or more. All charges are saturated with either an H–O or an H–O–C fluid phase, whose presence in the run products is marked by the occurrence of bubbles. All crystalline phases are idiomorphic and evenly distributed throughout the charges. Hornblende and, to a lesser extent, orthopyroxene and clinopyroxene can contain inclusions of glass and oxides. Some hornblendes from clinopyroxene-free charges have clinopyroxene cores, which are interpreted as having grown early, during hydration of the glass or melt; they are clearly disequilibrium phases and subsequently reacted with the hydrous liquid to yield stable hornblende. Minute inclusions of the Fe–Ti oxides (mainly magnetite) are often observed crowding plagioclase cores, artificially increasing the iron content of this mineral, as measured with the electron microprobe. The textural and compositional features of run products suggest a close approach to equilibrium, as observed in other crystallization experiments on felsic to intermediate compositions (Clemens *et al.*, 1986; Pichavant, 1987; Conrad *et al.*, 1988; Holtz *et al.*, 1992; Scaillet *et al.*, 1995; Scaillet & Evans, 1999).

Phase relations

The phase relations are shown in Fig. 3 for redox conditions at NNO + 2·5 and NNO – 1·5. Melt H_2O contents for H_2O-saturated conditions range between 7·9 and 8·9 wt % (Appendices A and B). At NNO + 2·5 (Fig. 3a), ilmenite is present all over the phase diagram and is the liquidus phase for H_2O-rich conditions, with clinopyroxene, hornblende and magnetite as near-liquidus phases. Plagioclase comes next in the sequence, followed by quartz, alkali feldspar, biotite and titanite, this last phase crystallizing only below 800°C. The orthopyroxene stability field is restricted to the high-temperature, H_2O-poor (<5 wt % H_2O) part of the phase diagram. Hornblende crystallizes up to ~870°C for H_2O-saturated conditions and is unstable for melt H_2O contents <4·5 wt %. The hornblende stability field does not extend to the solidus, indicating that hornblende would have to resorb by reaction with the melt upon cooling, as is also the case for orthopyroxene and clinopyroxene. Orthopyroxene is not stable at 850°C and below, and there is a small T–wt % H_2O in melt region where biotite and orthopyroxene coexist, suggesting that a reaction relationship between these two phases defines the orthopyroxene lower stability limit. The clinopyroxene stability field envelops that of orthopyroxene. The high-temperature stability limits of clinopyroxene and orthopyroxene are both above 900°C and have not been determined. The low-temperature stability limit of clinopyroxene is uncertain below 800°C (see Appendix A). The stability fields of clinopyroxene and hornblende partially overlap, suggesting that a reaction relationship involving clinopyroxene defines the upper stability limit of hornblende for H_2O in melt <6 wt %. Below 800°C, hornblende stability is limited by a reaction relationship involving biotite and possibly titanite.

Decreasing fO_2 from NNO + 2·5 to NNO – 1·5 produces major changes in the phase relations (Fig. 3b). Titanite and magnetite disappear from the stable phase assemblage. Ilmenite is the sole Fe–Ti oxide and is found in all run products. For near H_2O-saturated conditions, ilmenite, clinopyroxene and orthopyroxene are liquidus or near-liquidus phases. Hornblende comes next in the sequence, being followed by biotite, plagioclase, quartz and alkali feldspar in that order. The plagioclase saturation curve is lowered by ~75°C relative to oxidizing conditions. Hornblende has an upper stability limit of ~810°C, depressed by ~60°C relative to NNO + 2·5, and is stable down to the solidus (Fig. 3b). Hornblende crystallization requires melt H_2O contents >4 wt %. Both orthopyroxene and clinopyroxene have upper and lower stability limits located at lower temperatures than under oxidizing conditions, and their stability fields extend to H_2O-saturated conditions. The overlapping of the stability fields of pyroxenes with that of hornblende suggests that a reaction relationship between pyroxenes and hornblende controls the upper stability limit of hornblende for H_2O in melt between 8 and 4 wt %.

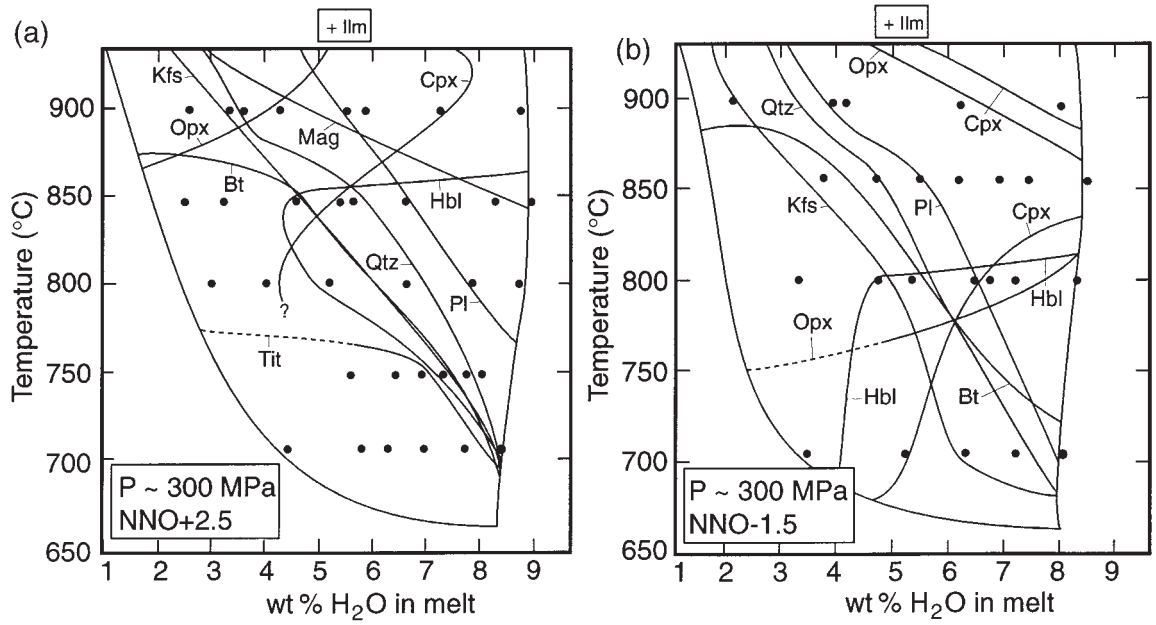

Fig. 3. Phase diagrams for the Jamon granite at ~300 MPa under (a) oxidized and (b) reduced conditions. Abbreviations as given by Kretz (1983). Uncertain portions of stability curves are indicated by dashed lines. (See text and Appendices A and B for experimental details.) Saturation curves are labelled with mineral names lying inside their stability field. Ilmenite is present in all run products in both diagrams.

Composition of experimental phases

Plagioclase

Representative plagioclase analyses are listed in Table 2. The variation of the anorthite content of plagioclase (An) with temperature and melt H_2O content is shown for the two sets of redox conditions investigated (Fig. 4). In both cases, An decreases with decreasing melt H_2O contents and temperature. As lowering fO_2 depresses the plagioclase saturation temperature, the composition of the first plagioclase to crystallize at a given temperature is less calcic under reduced than under oxidized conditions. For instance, at 900°C, the maximum An is $An_{\sim 47}$ for NNO + 2·5 and $An_{\sim 39}$ for NNO – 1·5 (Fig. 4). In contrast, for *T*–melt H_2O content conditions within the plagioclase stability field, plagioclase compositions under either reduced or oxidized conditions are identical.

Pyroxenes

Representative pyroxene compositions are listed in Table 3. Clinopyroxenes have Al_2O_3 contents between 1 and 3 wt % and Na_2O contents always $\leq$0·80 wt %. Clinopyroxenes fall in the field of augite (Morimoto *et al.*, 1988), except at 900°C (NNO + 2·5), where they have Wo contents >45 mol % and are therefore diopsides (Table 3). Clinopyroxenes crystallizing at NNO – 1·5 have Wo contents close to 30 mol % (Table 3) and are less calcic than those from the experiments at NNO + 2·5. The Fe/(Fe + Mg) ratio of clinopyroxene decreases with increasing temperature and fO_2. For both sets of redox conditions, this ratio is linearly correlated with temperature (Fig. 5). However, the trends are not parallel. The effect of temperature on Fe/(Fe + Mg) is more marked at NNO – 1·5.

Orthopyroxene compositions are characterized by Al_2O_3 contents <2·5 wt % at NNO + 2·5, <2 wt % at NNO – 1·5, and Wo contents <6 % (Table 3). Orthopyroxenes mostly have <50% Fs, except for NNO – 1·5 at 800°C and at 850°C in the most H_2O-undersaturated runs. As for clinopyroxenes, the Fe/(Fe + Mg) ratio of orthopyroxenes is affected by changes in both temperature and fO_2. In addition, at a given temperature and fO_2, decreasing the melt H_2O content strongly increases the Fe/(Fe + Mg) ratio in orthopyroxene.

Amphibole

Representative amphibole analyses are reported in Table 4. All are calcic amphiboles, being either ferrohornblendes at NNO – 1·5, or magnesiohornblendes at NNO + 2·5 (Leake *et al.*, 1997). The TiO_2 content varies little with temperature under both sets of redox conditions (Table 4). It increases slightly with decreasing fO_2, being in the range 1–1·6 wt % at NNO + 2·5, and 1–2 wt % at NNO – 1·5. K_2O content is always <1 wt % whereas Na_2O varies between 1·24 and 2 wt % at NNO + 2·5 and between 1·21 and 1·73 wt % at NNO – 1·5. Hornblendes crystallizing at low temperatures are, on

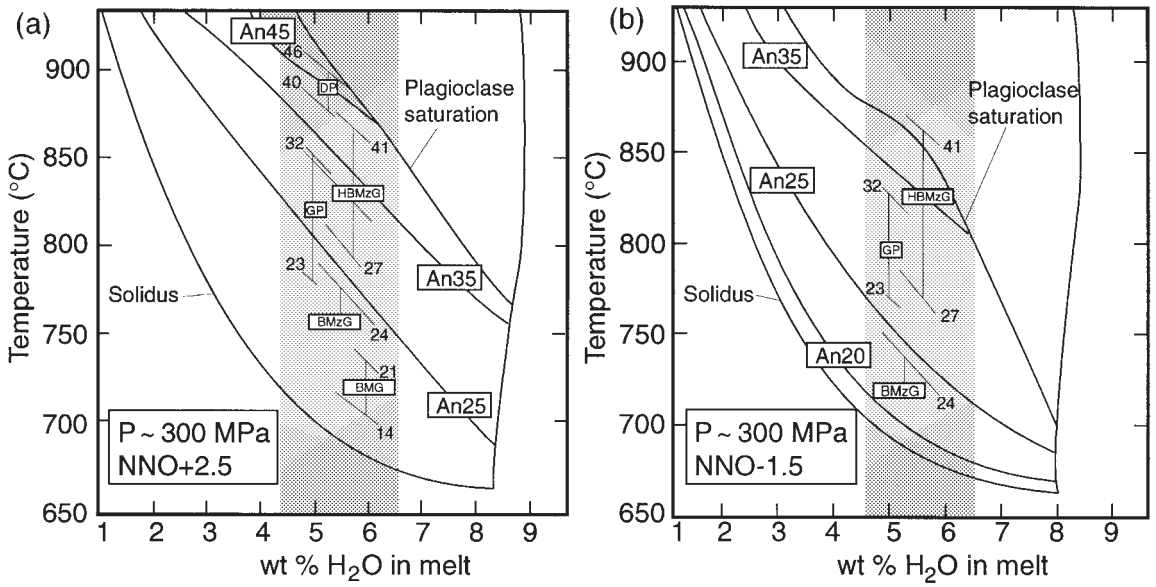

Fig. 4. An content of experimental plagioclases under (a) oxidized and (b) reduced conditions and comparison with An content of natural plagioclases (core compositions only) in the different facies. The stippled field corresponds to the range of melt H_2O content deduced from the comparison of the phase diagrams with the natural crystallization sequence. (See text for explanations.) Same abbreviations as in Fig. 1 and Table 1.

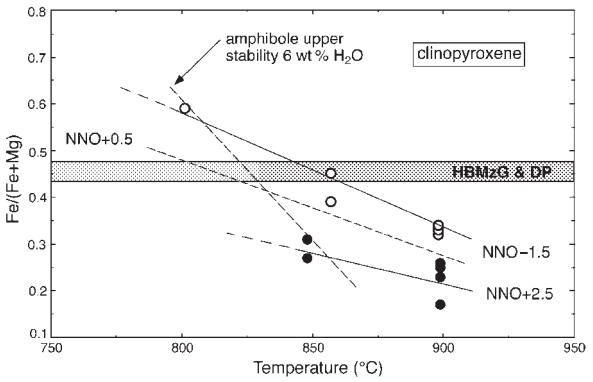

Fig. 5. Compositions of experimental clinopyroxenes in oxidized (●) and reduced (○) experiments compared with compositions of natural clinopyroxene inclusions in amphibole from the hornblende biotite monzogranite and dacite porphyry facies (stippled field). The dashed line marks the temperature of the upper stability limit of amphibole for 6 wt % H_2O in the melt (Fig. 3a, b). Clinopyroxene Fe/(Fe + Mg) ratios are consistent with temperatures of ~825°C for an fO_2 midway between the two experimental regression lines (NNO + 0·5). Same abbreviations as in Fig. 1 and Table 1.

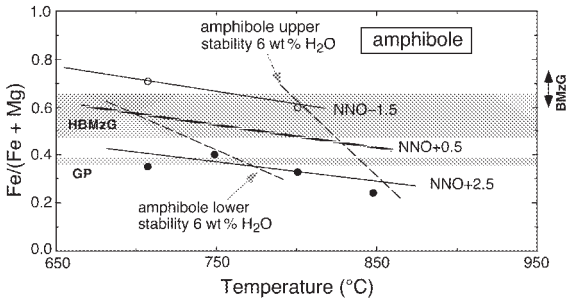

Fig. 6. Compositions of experimental amphiboles in oxidized (●) and reduced (○) experiments compared with compositions of natural amphiboles from the hornblende biotite monzogranite and rhyolite porphyry (stippled fields), and from the biotite monzogranite (compositional range indicated by an arrow). The dashed lines mark the hornblende upper and lower stability temperatures, respectively (Fig. 3a, b) for 6 wt % H_2O in the melt. Amphiboles from the hornblende biotite monzogranite facies have Fe/(Fe + Mg) ratios consistent with crystallization under approximately NNO + 0·5, although the more elevated Fe/(Fe + Mg) ratios probably correspond to re-equilibrated amphiboles, especially in the biotite monzogranite. Amphibole compositions from the rhyolite porphyry dykes indicate conditions more oxidizing than in the granite (NNO + 0·5 < fO_2 < NNO + 2·5). Same abbreviations as in Fig. 1 and Table 1.

average, poorer in Na_2O than those crystallizing at high temperatures (Table 4). The Al_2O_3 content is remarkably constant, being insensitive to variations in temperature, melt H_2O content and fO_2. The average Al_2O_3 content of our experimental amphiboles (Al_{tot} = 1·4) is intermediate between those calculated at 300 MPa using the geobarometers of Johnson & Rutherford (1989) and Schmidt (1992) (respectively, Al_{tot} of 1·53 and 1·26). The main compositional variation documented for our experimental hornblendes concerns again the Fe/(Fe + Mg) ratio (Fig. 6). As for pyroxenes, this ratio is strongly affected by changes in both fO_2 and temperature and, to a lesser extent, melt H_2O content. The Fe/(Fe + Mg) ratio increases with falling temperature and decreasing fO_2.

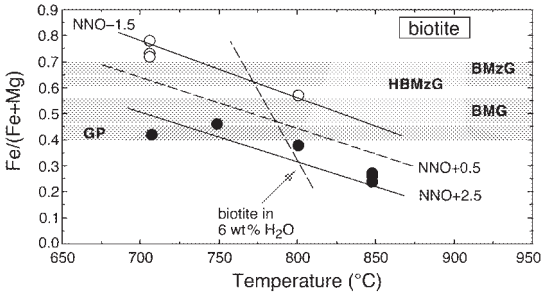

Fig. 7. Compositions of experimental biotites in oxidized (●) and reduced (○) experiments compared with compositions of natural biotites from the different facies (stippled fields). The biotite-in dashed line marks the temperature of appearance of biotite for 6 wt % H_2O in the melt (Fig. 3a, b). Biotite Fe/(Fe + Mg) compositions are consistent with crystallization at approximately NNO + 0·5, 700–730°C and 650–700°C, respectively, for the hornblende biotite monzogranite and biotite monzogranite. Biotite compositions in the rhyolite porphyry dykes suggest fO_2 conditions more oxidizing than in the granite, close to NNO + 2·5. (See text for discussion.) Same abbreviations as in Fig. 1 and Table 1.

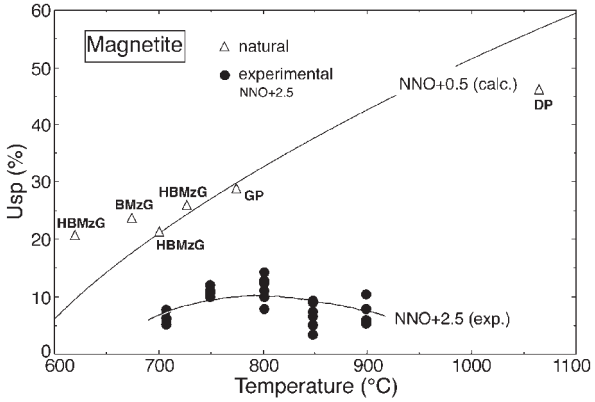

Fig. 8. Compositions of experimental (Table 6) and natural magnetites. The natural magnetites are reconstructed compositions (see Table 7). The NNO + 0·5 oxyisobar shows compositions of magnetite coexisting with ilmenite for NNO + 0·5, calculated from Spencer & Lindsley (1981). The significantly lower Usp contents in the experimental than in the natural magnetites should be noted; these suggest fO_2 conditions for the granite more reducing than NNO + 2·5. Same abbreviations as in Fig. 1 and Table 1.

Biotite

Owing to the small size of the crystals, analyses of all biotites were glass contaminated. Glass contribution was corrected for by assuming 1·7 of K per formula unit (for 22 oxygens) and normalizing oxide contents to a total of 96 wt % (see Scaillet *et al.*, 1995). Restored biotite analyses are listed in Table 5. The experimental biotites display elevated TiO_2 contents, in the range 3–5 wt %, except for the RD51 charge, whose biotite has a much higher TiO_2 (Table 5). This is possibly an artefact of the recalculation procedure or contamination with an oxide phase. Biotites show little or no octahedral Al. As for the other ferromagnesian silicates, the Fe/(Fe + Mg) ratio is inversely correlated with temperature, and increases when fO_2 decreases (Fig. 7).

Fe–Ti oxides

Representative oxide compositions are listed in Tables 6 (magnetite) and 7 (ilmenite). Glass contamination was corrected for by assuming no silica in the oxides. The content of Fe^{3+} was calculated from charge balance constraints. At NNO + 2·5, both magnetite and ilmenite are present. Magnetite is characterized by low Usp contents, from 3 to 15 mol %, depending on temperature (Table 6, Fig. 8). At all temperatures, Usp contents systematically decrease with increasing melt H_2O content. MgO increases regularly with temperature from 0·5 wt % at 700°C to 2·2 wt % at 900°C. The MnO content of magnetite is always <1 wt %, irrespective of the experimental conditions. Rhombohedral oxides crystallized at NNO + 2·5 have Ilm contents ranging from 25 mol % at 900°C to 40 mol % at 700–800°C (Table 7, Fig. 9). As for the coexisting magnetites, Ilm contents systematically decrease with increasing melt H_2O content. Their MnO content is <0·5 wt %, and MgO increases smoothly with temperature. At NNO – 1·5, only rhombohedral oxides are present and their Ilm contents range from 90 to 95 mol % (Table 7). At all conditions the MnO content is <1·5 wt %. MgO content is positively correlated with temperature but, compared with ilmenites crystallized at NNO + 2·5, those obtained at NNO – 1·5 are significantly more magnesian, with MgO contents reaching 3 wt % at 900°C. However, the redox effect on the MgO content progressively vanishes as temperature falls and both trends join at around 700°C.

Titanite

Titanite analyses could be obtained in several charges at 707°C and in one run at 749°C (NNO + 2·5). At 707°C, titanite has a TiO_2 content of 30–31 wt %, Al_2O_3 and FeO contents of 3 wt % each, and the oxides total 96 wt %. At 749°C, titanite is slightly depleted in TiO_2 (26 wt %) and enriched in Al_2O_3 (5 wt %).

DISCUSSION AND APPLICATION OF EXPERIMENTAL RESULTS

Comparison with previous work

The phase relations established by Clemens *et al.* (1986) for the Watergums granite, a representative of some southeastern Australian Palaeozoic A-type granites, differ in several aspects from the results of this study. The phase diagram for the Watergums granite lacks any

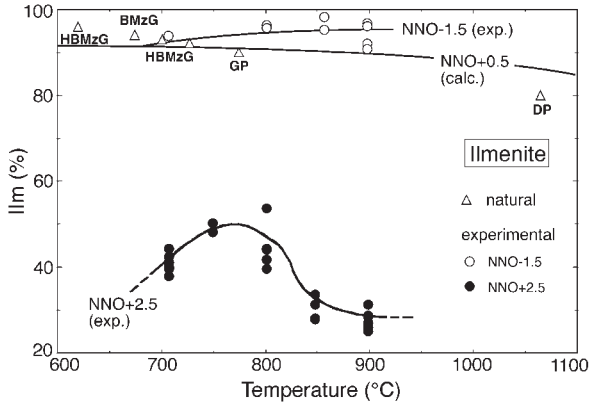

Fig. 9. Compositions of experimental (Table 7) and natural ilmenites. The natural ilmenite compositions plotted are the assumed primary ilmenite compositions of Dall'Agnol *et al.* (1997*a*) (see Table 7). Ilmenites from the oxidized experiments (NNO + 2·5) have markedly lower Ilm contents than the natural ilmenites. In contrast, ilmenite compositions from the reduced experiments (NNO – 1·5) have higher Ilm contents. It should be noted that for NNO – 1·5 ilmenite does not coexist with magnetite. The NNO + 0·5 oxyisobar shows compositions of ilmenite coexisting with magnetite for NNO + 0·5, calculated from Spencer & Lindsley (1981). Both natural and experimental ilmenite compositions are consistent with fO_2 ~ NNO + 0·5. Same abbreviations as in Fig. 1 and Table 1.

stability field for hornblende and is characterized by a very small biotite stability field. Saturation temperatures of quartz, plagioclase and alkali feldspar are markedly higher (Clemens *et al.*, 1986) than in this study (Fig. 3). Magnetite is the only Fe–Ti oxide present and no stability field exists for orthopyroxene (Clemens *et al.*, 1986). It should be noted that the Watergums granite composition is richer in SiO_2, and poorer in FeO_t, MgO, TiO_2 and CaO than the composition studied here. It is, however, virtually identical to the Jamon biotite monzogranite (Table 1), a fractionation product of the hornblende biotite monzogranite. Therefore, the differences between the two studies are mainly attributed to contrasted experimental conditions. Clemens *et al.* (1986) modelled the crystallization of a rather felsic, H_2O-undersaturated A-type magma under subvolcanic levels. Their experiments were carried out at 100 MPa, i.e. at a pressure probably too low to stabilize magmatic hornblende especially in a relatively Ca-poor composition (Naney, 1983). The low experimental pressure also explains the elevated saturation temperatures for quartz and feldspars found by Clemens *et al.* (1986), and possibly the small size of their biotite stability field. In terms of fO_2, the experiments of Clemens *et al.* (1986), although performed at NNO – 0·4, are characterized by the presence of magnetite, as found here for NNO + 2·5. The absence of ilmenite in their experiments (Clemens *et al.*, 1986) is probably due to the low TiO_2 content of the starting material (0·34 wt %), more than two times less than in the granite sample used in this study (0·80 wt %, Table 1). It is concluded that the two studies are essentially complementary, the present one extending the experimental database for A-type magmas to greater depths, more mafic compositions and different redox conditions.

One interesting aspect of the experimental results presented here concerns the stability relationships of ferromagnesian phases in granitic magmas *sensu lato*. Previously, this question was investigated by Naney (1983), who found that clinopyroxene and hornblende were mutually exclusive and that the presence of either phase was a strong function of bulk composition. In contrast, biotite, hornblende, clinopyroxene and orthopyroxene are found together in the experimental phase assemblages from this study, both at NNO + 2·5 and NNO – 1·5. The results confirm that biotite may be stable in granitic magmas over a large range of melt H_2O contents [Naney (1983) and references therein]. In this study, the biotite stability fields extend to melt H_2O concentrations as low as 2 wt % (Fig. 3a and b). In contrast, to be stable, hornblende requires minimum concentrations in the melt of 4–5 wt % H_2O (Fig. 3), irrespective of fO_2 and in excellent agreement with the minimum value of 4 wt % H_2O from the 200 MPa data of Naney (1983). Therefore, magmatic hornblende is a reliable indicator of relatively high minimum concentrations of H_2O in granitic magmas. In addition, hornblende stability is strongly dependent on fO_2. For NNO + 2·5 (Fig. 3a), hornblende has a lower stability limit, as found by Naney (1983) for NNO < fO_2 < HM at 200 and 800 MPa. Therefore, for hydrous (H_2O > 4 wt %) granitic magmas evolving under oxidizing conditions (> NNO), early crystallizing hornblende will be replaced upon cooling by biotite- and titanite-bearing (this study), or epidote-bearing (Naney, 1983) assemblages. The restriction of titanite to oxidizing conditions, as reported here, is consistent with the experimental results of Spear (1981), which demonstrate that, at 300 MPa, titanite is stable up to 800°C under redox conditions fixed by the HM buffer whereas, for fO_2 buffered at FMQ, the maximum stability of titanite does not exceed ~620°C. In contrast, for NNO – 1·5, hornblende is stable down to the solidus (Fig. 3b). Therefore, for granitic magmas evolving under reducing conditions (< NNO), hornblende may crystallize relatively late as a near-solidus phase. The lowering of the upper stability limit of hornblende relative to NNO + 2·5 is a consequence of the expansion of the stability fields of pyroxenes towards lower temperatures with decreasing fO_2. It is also worth noting that, at NNO – 1·5, the stability fields for both orthopyroxene and clinopyroxene extend to H_2O-saturated conditions (Fig. 3b). Thus, under reducing conditions, crystallization of pyroxene-bearing assemblages may simply indicate elevated temperatures and not necessarily dry conditions.

Phase assemblages and order of crystallization

The experimental results obtained under either reducing or oxidizing fO_2 may be compared with the petrographic and mineralogical data on the granite, to provide first-order constraints on temperature, redox conditions and melt H_2O content during crystallization of the Jamon granite. The phase assemblage crystallizing under reducing conditions (NNO – 1·5) is characterized by the absence of magnetite and titanite, and the stability of amphibole down to the solidus for high melt H_2O contents. Moreover, orthopyroxene, a phase never observed in the granite, is present irrespective of the melt H_2O content. All these results are inconsistent with the mineralogy of the Jamon granite.

In contrast, under more oxidizing conditions (NNO + 2·5), ilmenite and magnetite crystallize together, ilmenite being earlier than magnetite in the sequence. In the H_2O-rich part of the phase diagram, ilmenite, magnetite and clinopyroxene are the near-liquidus phases, in agreement with petrographic observations. With falling temperature, clinopyroxene is replaced by amphibole, itself replaced by biotite. Titanite is the last mafic phase to appear in the experimental sequence. These results are consistent with textural data and order of crystallization as deduced from petrographical observations (Fig. 2). It is concluded that the H_2O-rich oxidizing experiments best reproduce the phase assemblage and crystallization order of the Jamon granite. This does not mean, however, that the Jamon magma crystallized exactly at the fO_2 conditions of our oxidizing experiments (i.e. NNO + 2·5).

H_2O content of the Jamon magma and crystallization temperatures

To evaluate the H_2O content of the Jamon magma, the phase diagram obtained under oxidizing conditions (Fig. 3a) is used first. Tight constraints are provided by the respective position of the magnetite, plagioclase and amphibole saturation curves (Fig. 3a). Petrographic observations and mineralogical data show that plagioclase and hornblende began to crystallize almost simultaneously. As magnetite inclusions are common in both plagioclase and hornblende, the T–H_2O path followed by the Jamon magma must pass very close to the intersection of the plagioclase and amphibole saturation curves (Fig. 3a), implying H_2O contents of ~6·5 wt %. A minimum amount of ~4·5 wt % H_2O in the melt is necessary for amphibole to crystallize (Fig. 3a).

The melt H_2O content determined above is unaffected by a change in fO_2. Use of the reducing instead of the oxidizing phase diagram and applying the same line of reasoning (intersection of the plagioclase and amphibole saturation curves) yields the same value of the melt H_2O content (6·5 wt % H_2O, Fig. 3b). By analogy, 4 wt % H_2O is also a minimum for amphibole crystallization (Fig. 3b).

An additional source of information on the H_2O content of the magma is provided by plagioclase. Compositions of plagioclase from different facies of the Jamon granite are shown superimposed on the An isopleths constructed from the experimental data (Fig. 4). Plagioclase cores' An values generally decrease from the hornblende biotite monzogranite to the biotite monzogranite and to the biotite micromonzogranite, corresponding to crystallization temperatures becoming progressively lower in the same order (respectively 870–800, $\leq$770 and 750–720°C). Plagioclases from the rhyolite porphyry dykes occupy an intermediate position (Fig. 4), between the hornblende biotite monzogranite and the biotite monzogranite, consistent with the bulk chemistries of the respective rocks (Table 1). They yield crystallization temperatures between 850 and 770°C. The dacite porphyry dykes have plagioclase compositions yielding the highest crystallization temperatures (~900°C, Fig. 4), assuming that the experimental results obtained on the granite apply to these more mafic dykes. Plagioclase compositions more calcic than An_{40} (as observed in both the hornblende biotite monzogranite and dacite porphyry) are not experimentally reproduced under reducing conditions (Fig. 4). This is a further indication that the reducing experiments yield results inconsistent with the mineralogical data. Using the plagioclase An isopleths from the oxidizing experiments (Fig. 4a), crystallization of a plagioclase An_{41} (highest An content in the hornblende biotite monzogranite) implies a maximum melt H_2O content of 6·5–7 wt %, and An_{46} (highest An content in the dacite porphyry) a maximum of 5·5–6 wt % H_2O.

It is worth stressing that the range of melt H_2O content determined above concerns the early stages of crystallization of the Jamon magma, as the approach is based on early magmatic phases such as plagioclase and amphibole. In the same way, it is emphasized that the plagioclase temperatures deduced from Fig. 4 apply to the early stages of plagioclase crystallization. We have no experimental constraints to evaluate the near-solidus melt H_2O contents. If an isobaric closed-system fractionation is assumed, the H_2O content of the magma must increase along with progressive crystallization so that values >6·5 wt % H_2O are likely to have been reached near the solidus.

T–fO_2 conditions

Experiments at NNO + 2·5 yield phase assemblages matching the main mineralogical features of the granite. A study of the Fe–Ti oxides (Dall'Agnol *et al.*, 1997*a*)

concluded that the Jamon granite equilibrated at ~NNO + 0·5. The systematic occurrence of titanite in all Jamon granite facies and associated dacite and rhyolite porphyry dykes also suggests fO_2 in the range of the HITMQ buffer (Wones, 1989), i.e. NNO + 0·5 to NNO + 1. Below, compositional data for the ferromagnesian phases are used to provide more precise constraints on redox conditions and crystallization temperatures.

Experimental and natural clinopyroxene Fe/(Fe + Mg) ratios are compared in Fig. 5. At NNO + 2·5, clinopyroxene is unstable below 850°C for 6 wt % H_2O in the melt (Fig. 3a) and the natural compositions, to be experimentally reproduced, would require fO_2 lower than or approximately NNO + 0·5 (midway between the two fO_2 investigated). It should be noted that, for NNO + 0·5, Fe/(Fe + Mg) ratios of natural clinopyroxenes would imply temperatures of ~825°C, very close to the upper stability limit of amphibole (Fig. 5) and consistent with the natural occurrence of clinopyroxene as relics in amphibole.

Experimental and natural amphibole Fe/(Fe + Mg) compositions are compared in Fig. 6. Amphiboles from the hornblende biotite monzogranite have a minimum Fe/(Fe + Mg) ratio of 0·47. To be experimentally reproduced, this requires fO_2 > NNO – 1·5 (Fig. 6). For NNO + 0·5, amphibole with such an Fe/(Fe + Mg) ratio would crystallize at ~800°C, compatible with the T–fO_2 crystallization of clinopyroxene. The high Fe/(Fe + Mg) values found in the hornblende biotite and the biotite monzogranites (respectively up to 0·65 and 0·73) probably correspond to re-equilibrated amphiboles because they imply temperatures in the subsolidus region for NNO + 0·5 (Fig. 6). In contrast, the Fe/(Fe + Mg) ratios of amphiboles in the rhyolite porphyry dykes are much lower, suggesting higher fO_2 than in the granite (Fig. 6). For an fO_2 intermediate between NNO + 2·5 and NNO + 1·5, amphiboles in the rhyolite porphyry dykes would crystallize in the range 800–830°C (Fig. 6). Higher-fO_2 conditions in the dykes than in the granite explain the differences in mineral compositions and confirm the presence of various magmas with independent origins. However, this conclusion is based on the assumption that the compositions of amphiboles are representative of the high-temperature magmatic stage. This is probably reasonable in the case of the rhyolite porphyry dyke samples that were rapidly cooled, but more questionable for the hornblende biotite monzogranite. Amphibole Fe/(Fe + Mg) provides only minimum estimates of T and fO_2 if re-equilibrated.

Experimental and natural biotite compositions are compared in Fig. 7. Biotite Fe/(Fe + Mg) compositions are consistent with crystallization at NNO + 0·5, from 700–730°C (hornblende biotite monzogranite) to 680–710°C (biotite monzogranite). As for the amphiboles, the Mg-rich biotites in the rhyolite porphyry dykes suggest fO_2 intermediate between NNO + 2·5 and NNO + 0·5 and crystallization temperatures in the range 750–800°C (Fig. 7). The relatively Mg-rich biotites of the micromonzogranite probably reflect a late-magmatic, oxidizing evolution related to open-system degassing (e.g. Czamanske & Wones, 1973; Scaillet *et al.*, 1995; Pichavant *et al.*, 1996).

Compositions of experimental magnetites and ilmenites are shown projected in Figs 8 and 9, together with compositions of natural Fe–Ti oxides. The NNO + 0·5 oxyisobar shows compositions of coexisting Fe–T: oxides for NNO + 0·5, calculated from Spencer & Lindsley (1981). The natural magnetites have higher Usp contents than the experimental, suggesting fO_2 conditions more reducing than NNO + 2·5. The experimental ilmenites plot on either side of the natural compositions (Fig. 9), again indicating fO_2 conditions intermediate between NNO + 2·5 and NNO – 1·5. However, it should be stressed that the experimental ilmenites for NNO – 1·5 do not coexist with magnetite and, therefore, can be compared neither with the other experimental (NNO + 2·5) nor with the natural ilmenites. It is concluded that the experimental Fe–Ti oxide compositions are consistent with the fO_2 range deduced from the natural oxide pairs (i.e. NNO + 0·5, Dall'Agnol *et al.*, 1997*a*).

In summary, fO_2 conditions at NNO + 0·5, i.e. intermediate between the two experimentally investigated fO_2 values, would allow compositions of ferromagnesian phases to match the compositions of the granite. For this fO_2 range, temperatures deduced from the phase compositions are consistent both with the petrographic and textural observations, and with the phase diagram (Fig. 3a). The early magmatic stage is characterized by a clinopyroxene-bearing assemblage crystallizing down to ~825°C. Amphiboles with the lowest Fe/(Fe + Mg) yield crystallization temperatures of ~800°C, followed by biotite crystallization below 730°C. Both amphibole and biotite compositions suggest fO_2 in the rhyolite porphyry dykes intermediate between NNO + 0·5 and NNO + 2·5, i.e. more oxidizing than in the granite, and indicating that various magmas with different fO_2 and presumably different origins are involved. Redox conditions deduced from the experimental data and the natural Fe–Ti oxides are in agreement, except for the rhyolite porphyry dykes, where experiments suggest fO_2 conditions more oxidizing than the natural Fe–Ti oxides by about 1 log unit.

Implications for the evolution of A-type granite magmas

A-type granitic magmas are commonly considered to evolve under elevated temperatures (e.g. Collins *et al.*, 1982; Christiansen *et al.*, 1983; Clemens *et al.*, 1986;

King *et al.*, 1997), and the results for the Jamon granite strengthen this proposal. Both geochemical data (e.g. P_2O_5 and Zr concentrations) and mineral compositions consistently suggest temperatures >800°C for the early magmatic history of the Jamon granite. Apatite and zircon saturation temperatures (respectively 802 and 851°C for the hornblende biotite monzogranite) are in the same range as temperatures of crystallization of the early mineral phases. For melt H_2O contents and fO_2 as determined above, the presence of an early clinopyroxene-bearing assemblage requires temperatures of at least 825°C, and crystallization of the plagioclase cores temperatures as high as 870°C. Other mineral phases such as hornblende and the Fe–Ti oxides in the porphyry dykes (Dall'Agnol *et al.*, 1997*a*) preserve a record of magmatic temperatures higher than 800°C.

The range of melt H_2O contents found in this study (4·5–6·5 wt % H_2O) is higher than previous experimentally based estimates for A-type granites (2·4–4·3 wt % H_2O, Clemens *et al.*, 1986). Both this study and that of Clemens *et al.* (1986) yield the same range of aH_2O (~0·6–0·8) and suggest that A-type granite magmas should not be considered necessarily as exceptionally H_2O poor [see discussions by Clemens *et al.* (1986) and King *et al.* (1997)]. It is emphasized that the range of melt H_2O contents determined here applies to the early crystallization history of the granite. Epizonal granite plutons are typically emplaced in a nearly entirely molten state (e.g. Wall *et al.*, 1987; Scaillet *et al.*, 1998) and, in the case of the Jamon, there is neither field nor textural evidence for emplacement of a crystal-rich mush. Therefore, crystallization before magma emplacement at its current level was no more than a few per cent and the range of H_2O concentrations determined above can be taken as the range of melt H_2O contents in the zone of magma generation.

Perhaps the most controversial result from this study is the experimental confirmation of relatively oxidizing fO_2 (NNO + 0·5) during crystallization of the Jamon granite, in agreement with the Fe–Ti oxides data (Dall'Agnol *et al.*, 1997*a*) and with the systematic occurrence of titanite. It should be noted that experimental data indicate conditions still more oxidizing in the rhyolite porphyry dykes. Although fayalite is commonly found in many A-type granitoids (Clemens *et al.*, 1986; Rämö & Haapala, 1991, 1995; Emslie & Stirling, 1993), it has never been encountered in the Jamon granite. Therefore, all the available evidence suggests that the granite evolved under relatively oxidizing conditions throughout the magmatic history. This conclusion is in contrast to the moderately to strongly reducing conditions of evolution of many other A-type granites (e.g. Clemens *et al.*, 1986; Emslie & Stirling, 1993; Frost & Frost, 1997; King *et al.*, 1997). Therefore, the group of A-type granites includes members with a wide range of fO_2 (see Anderson & Bender, 1989; Anderson & Smith, 1995; Dall'Agnol *et al.*, 1997*a*). Assuming that the fO_2 values of granite magmas reflect those of their source regions (e.g. Carmichael, 1991; Pichavant *et al.*, 1996; Frost & Frost, 1997), then the diversity of A-type granites in terms of fO_2 implies major differences in the nature of their source rocks.

The Jamon granite belongs to the subgroup of aluminous A-type granites, as recently defined by King *et al.* (1997) on examples from the Lachlan Fold Belt. However, it evolved under more oxidizing conditions than most of these Australian aluminous A-type magmas. In fact, the Jamon granite is very close in age, tectonic setting and fO_2 to the Hualapai, St François Mountains and San Isabel anorogenic granites of southwestern USA (Anderson & Bender, 1989; Lowell, 1991; Anderson & Smith, 1995). Conclusions drawn here about the intensive factors and magmatic evolution apply to this specific subgroup of oxidized A-type granite magmas and should not be extended to other subgroups. The experimental data presented in this paper for NNO – 1·5 are probably applicable to the subgroup of reduced A-type granites.

Magma generation

The experiments presented here apply to the crystallization of the Jamon granite, after its emplacement at ~300 MPa, and consequently provide little direct insight into magma generation processes. However, constraints can be placed on the nature of the source rocks and conditions of partial melting. As a working hypothesis, the Jamon granite is considered as being directly produced by partial melting at middle- to lower-crustal depths [e.g. Anderson & Bender (1989) and references therein; see also Rämö & Haapala (1995)], rather than being the result of fractionation of a more mafic magma. From the petrographic and mineralogical data, the early magmatic history of the granite is characterized by an assemblage of essentially plagioclase, pyroxenes and oxides. These phases were shown to crystallize near the liquidus at 300 MPa (Fig. 3). They are likely to persist as near-liquidus phases at the pressure of magma generation, as the mineralogy of the granite bears no evidence for a distinct high-pressure phase assemblage. Thus, plagioclase, pyroxenes and Fe–Ti oxides must dominate the mineralogy of the residual source rocks left after partial melting. Residual rocks with such characteristics are mafic–intermediate granulites, most probably derived from igneous protoliths of intermediate composition. Various Archaean granitoids of the Rio Maria Granodiorite and Arco Verde Tonalite (Fig. 1) were tested as model sources, assuming that they are geochemically and mineralogically similar to the source rocks at depth. Both major- and trace-element modelling and Sm–Nd isotopic

data show that an Archaean (2878 ± 4 Ma) quartz diorite, present as enclaves in the granodiorite, is a suitable source for the Jamon granite (Dall'Agnol *et al.*, 1999*b*). The other granitoids tested yielded negative results (Dall'Agnol *et al.*, 1999*b*). The Rio Maria quartz diorite is composed of 47% (modal) plagioclase, 12% quartz, 23% hornblende and 16% biotite. Its bulk composition (Dall'Agnol *et al.*, 1999*b*) is poor in SiO_2 (55·17 wt %) and Al_2O_3 (14·13 wt %), and relatively rich in MgO (5·77 wt %), within the range of the metamorphosed basalts and andesites investigated experimentally by Beard & Lofgren (1991). Major and trace element concentrations (high Cr, Ni, Sr, Ba and LREE) suggest that the quartz diorite belongs to the sanukitoid suite, a suite of Mg-rich monzodioritic to granodioritic rocks that forms a subordinate fraction of the Archaean crust (Shirey & Hanson, 1984; Stern *et al.*, 1989; Stern & Hanson, 1991). According to the results of Beard & Lofgren (1991), dehydration melting of such a protolith between 300 and 690 MPa would yield plagioclase, pyroxenes (cpx > opx) and Fe–Ti oxides as residual phases, i.e. an assemblage consistent with the near-liquidus mineralogy of the granite. The quartz diorite contains magnetite, ilmenite and titanite (Dall'Agnol *et al.*, 1999*b*) and magmas generated from such sources will be relatively oxidized, in the same fO_2 range as the Jamon granite. The oxidized character of the quartz diorite and of other Archaean sanukitoids is consistent with their proposed origin as mantle-derived melts generated in oceanic convergent margins (Stern & Hanson, 1991). The greenstone belts (Fig. 1) were not tested as possible sources, because of the lack of sufficient data. However, they are composed of komatiites and tholeiitic basalts that are on average reduced (Frost & Frost, 1997) and will not have appropriately high fO_2 except if oxidized during a metamorphic event. The high fO_2 of the Jamon granite is most consistent with a protolith that was originally oxidized.

Partial melting and generation of A-type granite magmas has been commonly considered to take place under fluid-absent conditions (e.g. Christiansen *et al.*, 1983; Clemens *et al.*, 1986). In this model, H_2O necessary for melting is supplied by the breakdown of hydrous phases in the source region. Hornblende and biotite are the main hydrous phases in the quartz diorite protolith inferred to be a possible source for the Jamon granite. Neglecting in first approximation the effect of biotite, the experimental data of Beard & Lofgren (1991) show that liquids produced by dehydration melting of hornblende between 300 and 690 MPa, 900 and 1000°C, have H_2O contents between 1·96 and 5·85 wt %. Compositions of experimental melts (Beard & Lofgren, 1991) are close to the composition of the Jamon hornblende biotite monzogranite, although important differences exist for some oxides (Al_2O_3 higher by 1–2 wt % in the experimental glasses, K_2O lower by 2 wt %). Clemens & Vielzeuf (1987) have developed a general model for estimating the H_2O contents of melts generated by dehydration melting. In terms of hornblende–biotite modal proportions, the quartz diorite protolith considered here lies between the two model compositions of Clemens & Vielzeuf (1987), being more hornblende rich and mafic than their intermediate composition. Consequently, results for the quartz diorite source are expected to be intermediate between the two model compositions of Clemens & Vielzeuf (1987). Taking the H_2O content of the quartz diorite (1·2 wt %, Dall'Agnol *et al.*, 1999*b*) as the H_2O content of the source, melt H_2O contents at 900°C are 3–4·6 wt % respectively for the intermediate and mafic model compositions of Clemens & Vielzeuf (1987) at 500 MPa, and 5·5–7·5 wt % at 1000 MPa. This range of calculated melt H_2O contents is in agreement with that determined for the early magmatic history of the Jamon granite (4·5–6·5 wt % H_2O), especially if melting takes place at pressures >500 MPa. Therefore, data on melt H_2O contents provide permissive evidence for generation of the Jamon granite from a quartz diorite protolith. For 4·5–6·5 wt % H_2O in the melt and a source rock with 1·2 wt % H_2O, melt fractions range between 18 and 26 wt %. This is in good agreement with a melt fraction of 24 wt % obtained from geochemical calculations (Dall'Agnol *et al.*, 1999*b*). In the pressure range 300–700 MPa, experiments on mafic–intermediate lithologies similar to the quartz diorite have located the hornblende dehydration melting reactions either between 850 and 900°C (Beard & Lofgren, 1991), or between 900 and 925°C (Patiño Douce & Beard, 1995). This range of temperatures, which is a good estimate of the temperatures attained in the source region before magma extraction, is consistent with the conditions inferred for the early crystallization of the Jamon magma, and with the temperature of the amphibole upper stability limits (Fig. 3a). This demonstrates that dehydration melting involving a dominantly hornblende-bearing source rock satisfactorily accounts for both the H_2O content and magmatic temperatures of the Jamon granite.

Patiño Douce (1997) has emphasized melting of calc-alkaline granitoids at low pressures (depths ≤15 km or 400 MPa) as the most feasible mechanism for the origin of metaluminous A-type granites. Although precise constraints are lacking for the Jamon granite, pressures of magma generation >500 MPa are preferred here on the basis of the melt H_2O content calculations above. The field relations make difficult to accept that the Jamon granite was generated at only 100 MPa (or 200 MPa at most) beneath its emplacement level. The model of Patiño Douce (1997), which is based on the preferential stabilization of an opx + plag residual assemblage upon lowering pressure, applies mostly to subvolcanic felsic, reduced A-type granites associated with anorthosite–

norite–mangerite–charnockite complexes. It does not account well for some of the characteristics of the Jamon granite [comparatively low SiO_2 and high CaO, low K_2O/Na_2O, Sr ≫ 100 ppm, Table 1; see also Patiño Douce (1997)]. Experimental data presented in this paper (Fig. 3) show that fO_2 has a strong influence on stabilities of pyroxenes at a fixed pressure so that we are reluctant to accept that pressure is the only factor able to control restite mineralogy and compositions of melts formed by dehydration melting of biotite and amphibole. For example, Beard & Lofgren (1991) found that increasing pressure slightly increases the modal proportion of opx over cpx in the residues of dehydration melting of calc-alkaline basalts and andesites, i.e. the reverse of the pattern proposed by Patiño Douce (1997). It is also worth pointing out that the quartz diorite is distinctly less SiO_2 rich than the calc-alkaline granitoids (tonalites to granodiorites) considered as sources of A-type granites in the model of Patiño Douce (1997).

CONCLUSIONS

(1) Crystallization experiments were performed on a relatively mafic border facies of the Jamon massif, a representative of the Lower Proterozoic oxidized A-type granite of the eastern Amazonian craton. Experiments were carried out at 300 MPa between 700 and 900°C for various melt H_2O contents and for both oxidizing (NNO + 2·5) and reducing (NNO – 1·5) conditions. Experimental phase assemblages and compositions were compared with the petrographic and mineralogical data on the different facies of the granite, to provide constraints on temperature, redox conditions and melt H_2O content during crystallization.

(2) The experimental phase assemblage for reducing conditions is characterized by the absence of magnetite and titanite and by the presence of orthopyroxene, and is inconsistent with the mineralogy of the Jamon granite. In contrast, under oxidizing conditions, ilmenite and magnetite crystallize together with clinopyroxene, amphibole, biotite, titanite, quartz, alkali feldspar and plagioclase. In the H_2O-rich part of the phase diagram, the mineral assemblage of the granite is reproduced.

(3) Compositions of clinopyroxene, plagioclase and, to a lesser extent, amphibole all suggest elevated temperatures (higher than 800°C, up to 870°C) for the early magmatic history of the Jamon granite. Apatite and zircon saturation temperatures are in the same range as temperatures of crystallization of the early mineral phases. The results for the Jamon granite strengthen the proposal that A-type granites have elevated magmatic temperatures and are generated by high-temperature partial melting.

(4) Crystallization of amphibole provides a minimum value of melt H_2O content of 4·5 wt %, and the respective positions of the magnetite, plagioclase and amphibole saturation curves a maximum value of 6·5 wt % H_2O. This range of melt H_2O content is higher than previous estimates for some other A-type granites. However, both this study and that of Clemens *et al.* (1986) suggest that A-type granite magmas evolve under conditions that are H_2O undersaturated, but not exceptionally H_2O poor.

(5) Experimental phase assemblages and compositions provide demonstration of relatively oxidizing fO_2 (~NNO + 0·5) during crystallization of the Jamon A-type granite. This fO_2 range is in agreement with the data from natural Fe–Ti oxides, with the systematic occurrence of titanite in all Jamon granite facies, and with the lack of fayalite. This conclusion contrasts with most models for A-type granite magmatism. The group of A-type granites includes members with variable fO_2, a consequence of major differences in the nature of their source rocks. The Jamon granite belongs to the subgroup of oxidized aluminous A-type granites and conclusions drawn here about the intensive factors and magmatic evolution apply to this specific subgroup only.

(6) Plagioclase, pyroxenes and oxides are near-liquidus phases and they probably dominate the mineralogy of the residual source rocks left after magma extraction. Residual rocks with such characteristics are mafic–intermediate granulites and the Jamon granite was most probably generated from oxidized Archaean igneous rocks of mafic–intermediate composition. Fluid-absent partial melting involving a dominantly hornblende-bearing source rock satisfactorily accounts for both the H_2O content and early crystallization temperatures of the Jamon magma.

ACKNOWLEDGEMENTS

This study was supported by the Federal University of Pará and PADCT-FINEP (4/3/87/0911/00 and 6.5.92.0025.00). Professor M. Lelubre was a source of inspiration for the petrological interpretations. Thorough and constructive reviews were provided by J. D. Clemens, A. E. Patiño Douce and J. L. Anderson. We gratefully acknowledge the editorial handling of M. Wilson.

REFERENCES

Anderson, J. L. (1983). Proterozoic anorogenic granite plutonism of North America. In: Medaris, L. G., Jr, Byers, C. W., Mickelson, D. M. & Shanks, W. C. (eds) *Proterozoic Geology: Selected Papers from an International Proterozoic Symposium. Geological Society of America Memoir* **161,** 133–154.

Anderson, J. L. & Bender, E. E. (1989). Nature and origin of Proterozoic A-type granitic magmatism in the southwestern United States of America. *Lithos* **23,** 19–52.

Anderson, J. L. & Smith, D. R. (1995). The effects of temperature and fO_2 on the Al-in-hornblende barometer. *American Mineralogist* **80,** 549–559.

Barker, F., Wones, D. R., Sharp, W. N. & Desborough, G. A. (1975). The Pikes Peak batholith, Colorado Front Range, and a model for the origin of the gabbro–anorthosite–syenite–potassic granite suite. *Precambrian Research* **2,** 97–160.

Beard, J. S. & Lofgren, G. E. (1991). Dehydration melting and water-saturated melting of basaltic and andesitic greenstones and amphibolites at 1, 3 and 6·9 kbar. *Journal of Petrology* **32,** 365–401.

Bettencourt, J. S., Tosdal, R., Leite, W. B., Jr & Payolla, B. L. (1995). Overview of the rapakivi granites of the Rondônia Tin Province (RTP). In: Bettencourt, J. S. & Dall'Agnol, R. (eds) *Symposium on Rapakivi Granites and Related Rocks. Excursion Guide Volume*. Belém: Federal University of Pará, pp. 5–14.

Bridgwater, D. & Windley, B. F. (1973). Anorthosites, post-orogenic granites, acid volcanic rocks and crustal development in the North Atlantic Shield during the mid-Proterozoic. In: Lister, L. A. (ed.) *Symposium on Gneisses and Related Rocks. Geological Society of South Africa Special Publication* **3,** 303–317.

Burnham, C. W., Holloway, J. R. & Davis, N. F. (1969). Thermodynamic properties of water to 1000°C and 10000 bars. *Geological Society of America Special Paper* **132,** 96 pp.

Carmichael, I. S. E. (1991). The redox states of basic and silicic magmas: a reflection of their source regions? *Contributions to Mineralogy and Petrology* **106,** 129–141.

Chou, I. M. (1987). Oxygen buffer and hydrogen sensor techniques at elevated pressures and temperatures. In: Barnes, H. L. & Ulmer, G. C. (eds) *Hydrothermal Experimental Techniques*. New York: John Wiley, pp. 61–99.

Christiansen, E. H., Burt, D. M., Sheridan, M. F. & Wilson, R. T. (1983). Petrogenesis of topaz rhyolites from the western United States. *Contributions to Mineralogy and Petrology* **83,** 16–30.

Clemens, J. D. & Vielzeuf, D. (1987). Constraints on melting and magma production in the crust. *Earth and Planetary Science Letters* **86,** 287–306.

Clemens, J. D., Holloway, J. R. & White, A. J. R. (1986). Origin of an A-type granite: experimental constraints. *American Mineralogist* **71,** 317–324.

Collins, W. J., Beams, S. D., White, A. J. R. & Chappell, B. W. (1982). Nature and origin of A-type granites with particular reference to southeastern Australia. *Contributions to Mineralogy and Petrology* **80,** 189–200.

Conrad, W. K., Nicholls, I. A. & Wall, V. J. (1988). Water-saturated and undersaturated melting of metaluminous and peraluminous crustal compositions at 10 kb: evidence for the origin of silicic magmas in the Taupo Volcanic Zone, New Zealand, and other occurrences. *Journal of Petrology* **29,** 765–803.

Creaser, R. A., Price, R. C. & Wormald, R. J. (1991). A-type granites revisited: assessment of a residual-source model. *Geology* **19,** 163–166.

Czamanske, G. K. & Wones, D. R. (1973). Oxidation during magmatic differentiation, Finmarka complex, Oslo area, Norway. *Journal of Petrology* **14,** 349–380.

Dall'Agnol, R. (1987). Petrologic evolution of the magnetite-bearing anorogenic Jamon Granite, East Amazon, Brazil: an example of moderate fractional crystallization. In: *International Symposium of Granites and Associated Mineralizations (ISGAM), Extended Abstracts*. Salvador da Bahia: Superintendência de Geologia e Recursos Minerais (SGRM), pp. 217–219.

Dall'Agnol, R. & Magalhães, M. S. (1995). Geochemistry and petrogenesis of the anorogenic Jamon and Musa granites, eastern Amazonian craton, Brazil: implications for the genesis of A-type Proterozoic granites. In: Dall'Agnol, R., Macambira, M. J. B. & Costi, H. T. (eds) *Symposium on Rapakivi Granites and Related Rocks. Abstract Volume*. Belém: Federal University of Pará, pp. 22–23.

Dall'Agnol, R., Lafon, J.-M. & Macambira, M. J. B. (1994). Proterozoic anorogenic magmatism in the Central Amazonian Province, Amazonian craton: geochronological, petrological and geochemical aspects. *Mineralogy and Petrology* **50,** 113–138.

Dall'Agnol, R., Pichavant, M. & Champenois, M. (1997*a*). Iron–titanium oxide minerals of the Jamon granite, Eastern Amazonian region, Brazil: implications for the oxygen fugacity in Proterozoic, A-type granites. *Anais da Academia Brasileira de Ciências* **69,** 325–347.

Dall'Agnol, R., Rämö, O. T., Magalhães, M. S. & Macambira, M. J. B. (1997*b*). Archean granitoids as magma sources for the anorogenic Paleoproterozoic Jamon and Musa granites (Eastern Amazonian Craton): new constraints based on geochemical and Sm–Nd isotope data. In: *South American Symposium on Isotope Geology. Extended Abstracts*. Campos do Jordão: CPGEO– IG–USP, pp. 96–97.

Dall'Agnol, R., Souza, Z. S., Althof, F. J., Barros, C. E. M., Leite, A. A. S. & Jorge João, X. S. (1997*c*). General aspects of the granitogenesis of the Carajás metalogenic province. In: *International Symposium of Granites and Associated Mineralizations (ISGAM) 2. Excursions Guide*. Salvador da Bahia: Companhia Baiana de Pesquisa Mineral (CBPM), pp. 135–161.

Dall'Agnol, R., Magalhães, M. S. & Teixeira, N. P. (1999*a*). Rapakivi granites from Brazil and adjacent areas. *Precambrian Research* **95,** 9–39.

Dall'Agnol, R., Rämö, O. T., Magalhães, M. S. & Macambira, M. J. B. (1999*b*). Petrology of the anorogenic, oxidised Jamon and Musa granites, Amazonian craton: implications for the genesis of Proterozoic A-type granites. *Lithos* **46,** 431–462.

Devine, J. D., Gardner, J. E., Brack, H. P., Layne, G. D. & Rutherford, M. J. (1995). Comparison of microanalytical methods for estimating H_2O contents of silicic volcanic glasses. *American Mineralogist* **80,** 319–328.

Eby, G. N. (1992). Chemical subdivision of the A-type granitoids: petrogenetic and tectonic implications. *Geology* **20,** 641–644.

Emslie, R. F. (1991). Granitoids of rapakivi granite–anorthosite and related associations. *Precambrian Research* **51,** 173–192.

Emslie, R. F. & Stirling, J. A. R. (1993). Rapakivi and related granitoids of the Nain plutonic suite: geochemistry, mineral assemblages and fluid equilibria. *Canadian Mineralogist* **31,** 821–847.

Frost, C. D. & Frost, B. R. (1997). Reduced rapakivi-type granites: the tholeiite connection. *Geology* **25,** 647–650.

Gastal, M. C. P. (1987). Mapeamento e petrologia do maciço granitico Musa, Rio Maria, Sudeste do Pará. Ph.D Thesis, Federal University of Pará, Belém, 319 pp.

Gower, C. F., Rivers, T. & Brewer, T. S. (1990). Mid-Proterozoic Laurentia–Baltica: an overview of its geological evolution and a summary of the contributions made by this volume. In: Gower, C. F., Rivers, T. & Ryan, B. (eds) *Mid-Proterozoic Laurentia–Baltica. Geological Association of Canada Special Paper* **38,** 485–506.

Haapala, I. & Rämö, O. T. (1990). Petrogenesis of the rapakivi granites of Finland. In: Stein, H. J. & Hannah, J. L. (eds) *Ore-bearing Granite Systems; Petrogenesis and Mineralizing Processes. Geological Society of America Special Paper* **246,** 275–286.

Haapala, I. & Rämö, O. T. (1992). Tectonic setting and origin of the Proterozoic rapakivi granites of southeastern Fennoscandia. *Transactions of the Royal Society of Edinburgh: Earth Sciences* **83,** 165–171.

Hammarstrom, J. M. & Zen, E-an (1986). Aluminium in hornblende: an empirical igneous geobarometer. *American Mineralogist* **71,** 1297–1313.

Harrison, T. M. & Watson, E. B. (1984). The behaviour of apatite during crustal anatexis: equilibrium and kinetic considerations. *Geochimica et Cosmochimica Acta* **48,** 1467–1477.

Hollister, L. S., Grissom, G. C., Peters, E. K., Stowell, H. H. & Sisson, V. B. (1987). Confirmation of the empirical correlation of Al in

hornblende with pressure of solidification of calc-alkaline plutons. *American Mineralogist* **72,** 231–239.

Holtz, F., Pichavant, M., Barbey, P. & Johannes, W. (1992). Effects of H_2O on liquidus phase relations in the haplogranite system at 2 and 5 kbar. *American Mineralogist* **77,** 1223–1241.

Holtz, F., Behrens, H., Dingwell, D. B. & Johannes, W. (1995). Water solubility in haplogranitic melts. Compositional, pressure and temperature dependence. *American Mineralogist* **80,** 94–108.

Ishihara, S. (1981). The granitoid series and mineralization. *Economic Geology* **75,** 458–484.

Johnson, M. C. & Rutherford, M. J. (1989). Experimental calibration of the aluminium-in-hornblende geobarometer with application to Long Valley caldera (California). *Geology* **17,** 837–841.

King, P. L., White, A. J. R., Chappell, B. W. & Allen, C. M. (1997). Characterization and origin of aluminous A-type granites from the Lachlan Fold Belt, southeastern Australia. *Journal of Petrology* **38,** 371–391.

Kretz, R. (1983). Symbols for rock-forming minerals. *American Mineralogist* **68,** 277–279.

Landenberger, B. & Collins, W. J. (1996). Derivation of A-type granites from a dehydrated charnockitic lower crust: evidence from the Chaelundi complex, eastern Australia. *Journal of Petrology* **37,** 145–170.

Leake, B. E., Wooley, A. R., Arps, C. E. S., Birch, W. D., Gilbert, M. C., Grice, J. D., Hawthorne, F. C., Kato, A., Kish, H. J., Krivovichef, V. G., Linthout, K., Laird, J., Mandarino, J., Maresch, W. V., Nickel, E. H., Rock, N. M. S., Schumacher, J. C., Smith, D. C., Stephenson, N. C. N., Ungaretti, L., Whittaker, E. J. W. & Youzhi, G. (1997). Nomenclature of amphiboles. Report of the Subcommittee on Amphiboles of the International Mineralogical Association Commission on New Minerals and Mineral Names. *European Journal of Mineralogy* **9,** 623–651.

Lowell, G. (1991). The Butler Hill caldera: a mid-Proterozoic ignimbrite–granite complex. In: Haapala, I. & Condie, K. C. (eds) *Precambrian Granitoids—Petrogenesis, Geochemistry and Metallogeny. Precambrian Research* **51,** 245–263.

Macambira, M. J. B. (1992). Chronologie U–Pb, Rb–Sr, K–Ar et croissance de la croûte continentale dans l'Amazonie du sud-est; exemple de la région de Rio Maria, Province de Carajás, Brésil. PhD Thesis, University of Montpellier II, 212 pp.

Macambira, M. J. B. & Dall'Agnol, R. (1997). Zircon age for the Paleoproterozoic Jamon granites, SE de Carajas Province, Brazil: new evidence of rocks older than 3·1 Ga in the Amazonian craton. In: *South American Symposium on Isotope Geology. Extended Abstracts*. Campos do Jordão: CPGEO–IG–USP, pp. 186–187.

Machado, N., Lindenmayer, Z., Krogh, T. E. & Lindenmayer, D. (1991). U–Pb geochronology of Archean magmatism and basement reactivation in the Carajás area, Amazon shield, Brazil. *Precambrian Research* **49,** 329–354.

Magalhães, M. S. & Dall'Agnol, R. (1992). Estudos de minerais opacos e susceptibilidade magnética nos granitos Musa e Jamon (região de Rio Maria–SE do Pará) e suas implicações petrológicas. *Revista Brasileira de Geociências* **22,** 184–197.

Magalhães, M. S., Dall'Agnol, R., Sauck, W. A. & Luiz, J. G. (1994). Susceptibilidade magnética: um indicador da evolução petrológica de granitóides da Amazônia. *Revista Brasileira de Geociências* **24,** 139–149.

Morimoto, N., Fabries, J., Ferguson, A. K., Ginzburg, I. V., Ross, M., Seifert, F. A., Zussman, J., Aoki, K. & Gottardi, G. (1988). Nomenclature of pyroxenes. *American Mineralogist* **73,** 1123–1133.

Naney, M. T. (1983). Phase equilibria of rock-forming ferromagnesian silicates in granitic systems. *American Journal of Science* **283,** 993–1033.

Nurmi, P. A. & Haapala, I. (1986). The Proterozoic granitoids of Finland: granite types, metallogeny, and relation to crustal evolution. *Geological Society of Finland Bulletin* **58,** 203–233.

Patiño Douce, A. E. (1997). Generation of metaluminous A-type granites by low-pressure melting of calc-alkaline granitoids. *Geology* **25,** 743–746.

Patiño Douce, A. E. & Beard, J. S. (1995). Dehydration-melting of biotite gneiss and quartz amphibolite from 3 to 15 kbar. *Journal of Petrology* **36,** 707–738.

Pichavant, M. (1987). Effects of B and H_2O on liquidus phase relations in the haplogranite system. *American Mineralogist* **72,** 1056–1070.

Pichavant, M., Hammouda, T. & Scaillet, B. (1996). Control of redox state and Sr isotopic composition of granitic magmas: a critical evaluation of the role of source rocks. *Transactions of the Royal Society of Edinburgh: Earth Sciences* **88,** 321–329.

Pimentel, M. M. & Machado, N. (1994). Geocronologia U–Pb dos terrenos granito–greenstone de Rio Maria, Pará. *38th Brasilian Congress of Geology, São Paulo, 1994, Abstract Volume*. São Paulo: pp. 390–391.

Pollard, P. J. & Mitchell, L. C. (1995). Metallogenic potential of Proterozoic rapakivi granites and related mafic rocks in the Cloncurry district, Mt. Isa inlier, Australia. In: Dall'Agnol, R., Macambira M. J. B. & Costi, H. T. (eds) *Symposium on Rapakivi Granites and Related Rocks. Abstract Volume*. Belém: Federal University of Pará, p. 64.

Rämö, O. T. & Haapala, I. (1991). The rapakivi granites of eastern Fennoscandia: a review with insights into their origin in the light of new Sm–Nd isotopic data. In: Gower, C. F., Rivers, T. & Ryan, B. (eds) *Mid-Proterozoic Laurentia–Baltica. Geological Association of Canada Special Paper* **38,** 401–415.

Rämö, O. T. & Haapala, I. (1995). One hundred years of rapakivi granite. *Mineralogy and Petrology* **52,** 129–185.

Robie, R. A., Hemingway, B. S. & Fisher, J. R. (1978). Thermodynamic properties of of minerals and related substances at 298·15 K and 1 bar (10^5 pascal) pressure and at higher temperatures. *US Geological Survey Bulletin* **1452,** 456 pp.

Scaillet, B. & Evans, B. W. (1999). The June 15, 1991 eruption of Mount Pinatubo. I. Phase equilibria and pre-eruption P–T–fO_2–fH_2O conditions of the dacite magma. *Journal of Petrology* **40,** 381–411.

Scaillet, B., Pichavant, M., Roux, J., Humbert, G. & Lefèvre, A. (1992). Improvements of the Shaw membrane technique for measurement and control of fH_2 at high temperatures and pressures. *American Mineralogist* **77,** 647–655.

Scaillet, B., Pichavant, M. & Roux, J. (1995). Experimental crystallization of leucogranite magmas. *Journal of Petrology* **36,** 663–705.

Scaillet, B., Holtz, F. & Pichavant, M. (1998). Phase equilibrium constraints on the viscosity of silicic magmas 1. Volcanic–plutonic comparison. *Journal of Geophysical Research* **103,** 27257–27266.

Schmidt, M. W. (1992). Amphibole composition in tonalite as a function of pressure: an experimental study at 650°C. *Contributions to Mineralogy and Petrology* **110,** 304–310.

Shaw, H. R. & Wones, D. R. (1964). Fugacity coefficients for hydrogen gas between 0 and 1000°C for pressures to 3000 atm. *American Journal of Science* **262,** 918–929.

Shirey, S. B. & Hanson, G. N. (1984). Mantle-derived Archean monzodiorites and trachyandesites. *Nature* **310,** 222–224.

Spear, F. S. (1981). An experimental study of hornblende stability and compositional variability in amphibolite. *American Journal of Science* **281,** 697–734.

Spencer, K. J. & Lindsley, D. H. (1981). A solution model for coexisting iron–titanium oxides. *American Mineralogist* **66,** 1189–1201.

Stern, R. A. & Hanson, G. N. (1991). Archean high-Mg granodiorite: a derivative of light rare earth element-enriched monzodiorite of mantle origin. *Journal of Petrology* **32,** 201–238.

Stern, R. A., Hanson, G. N. & Shirey, S. B. (1989). Petrogenesis of mantle-derived, LILE-enriched Archean monzodiorites and trachyandesites (sanukitoids) in southwestern Superior Province. *Canadian Journal of Earth Sciences* **26,** 1688–1712.

Stormer, J. C. (1983). The effects of recalculation on estimates of temperature and oxygen fugacity from analyses of multi-component iron–titanium oxides. *American Mineralogist* **68,** 586–594.

Van Schmus, W. R., Bickford, M. E. & Zietz, I. (1987). Early and Middle Proterozoic provinces in the central United States. In: Kröner, A. (ed.) *Proterozoic Lithospheric Evolution. American Geophysical Union, Geodynamic Series* **17,** 43–68.

Wall, V. J., Clemens, J. D. & Clarke, D. B. (1987). Models of granitoid evolution and source compositions. *Journal of Geology* **95,** 731–749.

Watson, E. B. & Harrison, T. M. (1983). Zircon saturation revisited: temperature and composition effects in a variety of crustal magma types. *Earth and Planetary Science Letters* **64,** 295–304.

Whalen, J. W., Currie, K. L. & Chappell, B. W. (1987). A-type granites: geochemical characteristics, discrimination and petrogenesis. *Contributions to Mineralogy and Petrology* **95,** 407–419.

Wones, D. R. (1989). Significance of the assemblage titanite + magnetite + quartz in granitic rocks. *American Mineralogist* **74,** 744–749.

Wyborn, L. A. I., Wyborn, D., Warren, R. G. & Drummond, B. J. (1992). Proterozoic granite types in Australia: implications for lower crust composition, structure and evolution. *Transactions of the Royal Society of Edinburgh: Earth Sciences* **83,** 201–209.

APPENDIX A

Table A: Experimental results for the Jamon granite under oxidizing conditions

Charge	XH_2O_{in}*	Results†	H_2O‡ in glass (wt %)	ΔNNO§
P *3129 bar,* T *801°C, run duration 498 h*				
RD1	1·00	Gl, Fl, Hbl, Ilm, Mag, (Cpx)	8·7	2·37
RD2	0·90	Gl, Fl, Hbl, Ilm, Mag	7·8	2·09
RD3	0·82	Gl, Fl, Hbl, Ilm, Mag, Pl, Qtz, (Cpx)	6·3	1·92
RD4	0·69	Gl, Fl, Hbl, Ilm, Mag, Pl, Qtz, Kfs, Bt, (Cpx)	5·2	1·73
RD5	0·60	Gl, Fl, Cpx, Ilm, Mag, Pl, Qtz, Kfs, Bt	*4·0*	1·64
RD6	0·50	Gl, Fl, Cpx, Ilm, Mag, Pl, Qtz, Kfs, Bt	*2·9*	1·44
P *3135 bar,* T *707°C, run duration 1023 h*				
RD7	1·00	Gl, Fl, Hbl, Ilm, Mag, Pl, (Cpx)	8·4	2·79
RD8	0·96	Gl, Fl, Cpx, Ilm, Mag, Bt, Pl, Qtz, Kfs, Tit	7·7	2·78
RD9	0·88	Gl, Fl, Ilm, Mag, Pl, Qtz, Kfs, Tit	*6·3*	*2·68*
RD10	0·85	Gl, Fl, Cpx, Ilm, Mag, Bt, Pl, Qtz, Kfs, Tit	*5·8*	*2·65*
RD11	0·80	Gl, Fl, Ilm, Mag, Pl, Qtz, Kfs, Tit	*4·9*	*2·60*
RD12	0·77	Gl, Fl, Cpx, Ilm, Mag, Bt, Pl, Qtz, Kfs	*4·4*	2·42
RD14	0·92	Gl, Fl, Cpx, Ilm, Mag, Bt, Pl, Qtz, Kfs	7·0	2·64
P *3100 bar,* T *848°C, run duration 329 h*				
RD15	1·00	Gl, Fl, Hbl, Ilm, (Cpx)	8·9	*3·12*
RD16	0·92	Gl, Fl, Hbl, Ilm, Mag, (Cpx)	8·3	3·05
RD17	0·79	Gl, Fl, Hbl, Ilm, Mag, Pl	6·6	2·81
RD18	0·68	Gl, Fl, Hbl, Ilm, Mag, Pl, Qtz	5·4	2·80
RD19	0·59	Gl, Fl, Hbl, Ilm, Mag, Pl, Qtz, (Cpx)	5·6	2·59
RD20	0·51	Gl, Fl, Hbl, Ilm, Mag, Pl, Qtz, Kfs, Cpx, Bt	*4·4*	2·47
RD21	0·38	Gl, Fl, Ilm, Mag, Pl, Qtz, Kfs, Cpx, Bt	*3·2*	2·19
RD22	0·29	Gl, Fl, Ilm, Mag, Pl, Qtz, Kfs, Cpx, Bt	*2·4*	2·23
P *3220 bar,* T *899°C, run duration 166 h*				
RD31	1·00	Gl, Fl, Ilm	8·7	*3·20*
RD32	0·91	Gl, Fl, Ilm, Cpx	7·2	*3·12*
RD33	0·79	Gl, Fl, Ilm, Cpx	5·8	*3·00*
RD34	0·70	Gl, Fl, Ilm, Cpx	5·6	*2·89*
RD35	0·60	Gl, Fl, Ilm, Mag, Cpx, Pl	4·2	2·76
RD36	0·51	Gl, Fl, Ilm, Mag, Cpx, Pl, Opx	3·5	2·68
RD37	0·40	Gl, Fl, Ilm, Mag, Cpx, Pl, Opx, Qtz	3·3	2·38
RD38	0·31	Gl, Fl, Ilm, Mag, Cpx, Pl, Opx, Qtz, Kfs	2·8	2·01
P *3086 bar,* T *749°C, run duration 449 h*				
RD40	0·96	Gl, Fl, Hbl, Ilm, Mag, Pl	*8·1*	2·08
RD41	0·90	Gl, Fl, Hbl, Ilm, Mag, Pl, Qtz,	7·7	1·97
RD42	0·85	Gl, Fl, Hbl, Ilm, Mag, Pl, Qtz, Kfs, Bt, (Cpx)	*7·4*	1·99
RD43	0·80	Gl, Fl, Ilm, Mag, Pl, Qtz, Kfs, Tit, Bt, Cpx	*7·0*	1·91
RD44	0·72	Gl, Fl, Ilm, Mag, Pl, Qtz, Kfs, Bt, Cpx	*6·4*	1·77
RD45	0·60	Gl, Fl, Ilm, Mag, Pl, Qtz, Kfs, Bt, Cpx	*5·6*	*1·68*

*$XH_2O_{in} = H_2O/(H_2O + CO_2)$ loaded in the capsule (in moles).
†Mineral abbreviations as given by Kretz (1983). Parentheses indicate a phase that is present either as an inclusion only (clinopyroxene in hornblende) or as a quench product (biotite).
‡Water contents of glasses determined using the by-difference method (Devine *et al.*, 1995). Numbers in italics indicate charges for which the melt water content was estimated using the correlation between XH_2O_{in} and the melt water content as established from neighbouring charges whose glass composition could be determined, allowing the use of the by-difference method.
§ΔNNO = log fO_2 (experiment) – log fO_2 (NNO; Chou, 1987). Experimental log fO_2 calculated using magnetite compositions and the empirical calibration between fO_2 and magnetite composition of Scaillet & Evans (1999) obtained at 780°C and 220 MPa. Numbers in italics are the fO_2 of charges lacking either one oxide or correct probe analyses of oxides. For these, when fO_2 at H_2O saturation is unknown (e.g. at 899°C), a maximum possible fO_2 is calculated as log fO_2 = log $fO_{2(exp)}$ + 2 log XH_2O_{in} in which log $fO_{2(exp)}$ corresponds to the fO_2 of the next nearest charge obtained from oxide composition (e.g. charge RD35 for calculating the fO_2 of charge RD34). When fO_2 at H_2O saturation is known, the relationship used is log fO_2 = log $fO_{2(aH_2O=1)}$ − 2 log XH_2O_{in} (e.g. charge RD7 for calculating the fO_2 of RD9).

APPENDIX B

Table B: Experimental results for the Jamon granite under reducing conditions

Charge	XH_2O_{in}*	Results†	H_2O‡ in glass (wt %)	ΔNNO§
P_t *2989 bar,* PH_2 *46 bar,* T *706°C, run duration 837 h*				
RD23	1·00	Gl, Fl, Hbl, Bt, Ilm, (Cpx)	8·1	−1·35
RD24	0·95	Gl, Fl, Hbl, Bt, Ilm, Pl, Qtz, (Cpx)	7·2	−1·40
RD25	0·90	Gl, Fl, Hbl, Bt, Ilm, Pl, Qtz,	*6·3*	−1·44
RD26	0·84	Gl, Fl, Hbl, Bt, Ilm Pl, Qtz, Kfs, Cpx	*5·2*	−1·50
RD28	0·75	Gl, Fl, Bt, Ilm, Pl, Qtz, Kfs, Cpx	*3·6*	−1·60
P_t *3035 bar,* PH_2 *45 bar,* T *801°C, run duration 331 h*				
RD46	1·00	Gl, Fl, Hbl, Ilm, (Bt)	8·2	−1·15
RD47	0·89	Gl, Fl, Hbl, Opx, Ilm	7·2	−1·25
RD48	0·81	Gl, Fl, Hbl, Ilm, Opx(?), (Cpx)	6·7	−1·33
RD49	0·70	Gl, Fl, Hbl, Ilm, Opx, Cpx, Pl	6·5	−1·46
RD50	0·61	Gl, Fl, Hbl, Ilm, Opx, Cpx, Pl, Qtz, Bt	5·3	−1·56
RD51	0·50	Gl, Fl, Hbl, Ilm, Opx, Cpx, Pl, Qtz, Bt, Kfs	*4·8*	−1·75
RD53	0·30	Gl, Fl, Ilm, Opx, Cpx(?), Pl, Qtz, Bt, Kfs	*3·4*	−2·19
P_t *3094 bar,* PH_2 *50 bar,* T *857°C, run duration 265 h*				
RD54	1·00	Gl, Fl, Opx, Cpx, Ilm, (Bt)	8·4	−1·11
RD55	0·90	Gl, Fl, Opx, Cpx, Ilm, (Bt)	7·4	−1·20
RD56	0·79	Gl, Fl, Opx, Cpx, Ilm	6·9	−1·31
RD57	0·73	Gl, Fl, Opx, Cpx, Ilm	6·1	−1·38
RD58	0·60	Gl, Fl, Opx, Cpx, Ilm, Pl	5·4	−1·55
RD59	0·51	Gl, Fl, Opx, Cpx, Ilm, Pl, Qtz	4·6	−1·69
RD61	0·30	Gl, Fl, Opx, Cpx(?), Ilm, Pl, Qtz, Bt	3·7	−2·15
P_t *3230 bar,* PH_2 *48 bar,* T *898°C, run duration 291 h*				
RD63	1·00	Gl, Fl, Ilm, (Bt)	7·9	−0·96
RD64	0·80	Gl, Fl, Ilm, Opx, Cpx, (Bt)	6·2	−1·15
RD65	0·60	Gl, Fl, Ilm, Opx(?), Cpx	4·3	−1·40
RD66	0·53	Gl, Fl, Ilm, Opx, Cpx	3·8	−1·51
RD68	0·29	Gl, Fl, Ilm, Opx, Cpx, Pl, Qtz, Kfs	2·1	−2·03

*$XH_2O_{in} = H_2O/(H_2O + CO_2)$ loaded in the capsule (in moles).
†Mineral abbreviations as given by Kretz (1983). Parentheses indicate a phase that is present either as an inclusion (clinopyroxene in hornblende) or as a quench product (biotite). The question mark indicates phases whose presence is strongly suspected but that could not be readily probed because of the fine grain size or intergrowth textures (mainly between Opx and Cpx).
‡Water contents of glasses determined using the by-difference method (Devine *et al.*, 1995). Numbers in italics indicate charges for which the melt water content was estimated using the correlation between XH_2O_{in} and the melt water content as established from neighbouring charges whose glass composition could be determined, allowing the use of the by-difference method.
§$\Delta NNO = \log fO_2$(experiment) – $\log fO_2$ (NNO; Chou, 1987). For H_2O-saturated conditions, fO_2 is calculated using the equation $fO_2 = (fH_2O°/(Kw \times PH_2)^2$ with $fH_2O°$ from Burnham *et al.* (1969), *Kw* from Robie *et al.* (1978) and the experimental PH_2. For H_2O-undersaturated charges, a maximum possible fO_2 is calculated as $\log fO_2 = \log fO_{2(aH_2O=1)} - 2 \log XH_2O_{in}$.